FINAL TECHNICAL REPORT

Award Number: G09AP00139

Ground Motion Simulations for the 1811 and 1812 New Madrid Earthquakes

Final Report

January 31, 2012

Sidao Ni, Paul Somerville and Robert Graves
(Contact Email: Paul.Somerville@urs.com)

URS Group, Inc.

915 Wilshire Boulevard, Suite 700

Los Angeles, CA 90017 U.S.A.

Tel: 213 996 2220, Fax: 213 996 2290

Abstract

The New Madrid earthquakes of 1811-1812 are the largest earthquakes to have struck the Central and Eastern United States (CEUS) in historic times. Magnitude estimates for these events vary from Mw 7 to 8, with median estimates of Mw 7.5 – 7.7 (Petersen et al., 2008). Clearly, if these types of events were to occur again, the impact to the built environment could be devastating. Over the last few years, important new information has been obtained regarding source characterization, wave propagation effects and site response in the New Madrid area. Additionally, recent advances in earthquake simulation algorithms and computational resources now allow us to compute realistic estimates of ground shaking from large earthquakes over a very large spatial extent. The main focus of this project is to provide quantitative estimates of the ground motions that were experienced in the greater New Madrid region during the three major earthquakes of 1811 and 1812. Using broadband ground motion simulation procedures, we estimate the ground motions that were generated by these earthquakes using the most up-to-date information available for these ruptures. We first determine fault plane parameters for the three main shocks from seismicity, scaling laws and previous studies. Then we generate rupture models for nine scenario earthquakes occurring on the three faults. Using the community velocity model of Central US (cusvm1.2), we compute 3D broadband seismograms with a hybrid approach featuring deterministic low frequency modeling with finite difference method and stochastic high frequency modeling with ray theory. Since little is known about the details of the rupture process during these earthquakes, we examine the sensitivity of the ground motion response to key elements of the source characterization, such as slip distribution, rupture velocity and hypocenter location. The sensitivities are analyzed over the computed ground motions after baseline trend is removed, and we find that the above mentioned elements all play important roles in affecting the ground motion. The simulated ground motions are quite consistent with the form of the Somerville et al. (2001) attenuation model, which is one of the models used in the generation of the USGS National Seismic Hazard Maps.

1. The 1811 and 1812 New Madrid Earthquakes

The New Madrid earthquakes of 1811 and 1812 have been studied extensively in recent years. These investigations include analysis of event magnitude (e.g., Hough et al., 2000; Bakun and Hooper, 2004; Johnston, 1996), shaking intensity (e.g., Nuttli, 1973; Hough et al, 2000), paleoseismic recurrence (e.g., Kelson et al., 1992; Tuttle et al., 1999), and velocity structure (e.g., Langston, 1994; Catchings, 1999; Saikia et al., 2006). In the latest version of the National Seismic Hazard Maps, median magnitude estimates for these three earthquakes are set between Mw 7.5 and 7.7 (Petersen et al., 2008), making them the largest earthquakes to occur in the CEUS in historic times.

The New Madrid seismic zone is an area of active seismicity, with the locations of the causative faults of the 1811-1812 events inferred from current background activity (Figure 1, Johnston and Schweig, 1996; Hough et al., 2000). Locations of the mainshock epicenters are inferred from intensity data (Johnston and Schweig, 1996). Hough et al (2000) reexamined the available intensity data for these events and present the most up-to-date perspective of the ground shaking that occurred during these ruptures. Figure 1 shows modified Mercalli intensities for the February 7, 1812 event, and implies maximum intensity of VIII in the near-source region, although based on very few data. However, intensities as high as V are reported along the eastern seaboard, several hundreds of km from the epicentral region. Not only does this imply low attenuation of ground motion with distance, but it also suggests that the events did not rupture close to the ground surface, hence mitigating very high intensities in the near-source region.

Previous ground motion simulations for New Madrid earthquakes have concentrated on point estimates of ground shaking at specific sites. Saikia and Somerville (1997) estimated ground motions in St. Louis for Mw 6.5 – 7.5 events in the New Madrid seismic zone. Toro and Silva (2001) and Atkinson and Beresnev (2002) estimate ground motions in St. Louis and Memphis for scenario New Madrid ruptures generally ranging from Mw 7.5 - 8. These studies find a general level of agreement with the observed intensity data for events having magnitudes of about 7.5. Ruptures with larger magnitudes produce intensities that exceed the observed levels in these locations.

2. Rupture Models of 1811 and 1812 Earthquakes

2.1 Fault plan parameters

The current USGS characterization of these events is summarized in Table 1 (Petersen et al., 2008). The fault models assume a depth to top of rupture of 10 km (qualitatively consistent with the near-source intensity data) and a maximum seismogenic thickness of 15 km (25 km depth). The magnitudes and rupture areas of these events are quite consistent with scaling relations for CEUS (Figure 3; Somerville et al., 2001). The shallow dip of the central segment is inferred from the distribution of current seismicity (see Figure 1).

Table 1. Source Parameters for 1811 and 1812 New Madrid earthquakes (Petersen et al., 2008)

Event	Segment	Median Mw	Strike	Dip	Rupture Area (km^2)*
Dec. 16, 1811	south	7.7	232	90	1920
Jan. 23, 1812	north	7.5	223	90	1050
Feb. 7, 1812	central	7.7	173	38	1500

*Rupture area assumes 15 km seismogenic thickness.

Figure 2 shows proposed fault orientations for the 1811-1812 scenarios developed by Leo Ramirez-Guzman along with recent seismicity. These fault orientations are similar to the ones we originally proposed based on the rough geometry given by Macpherson et al. (2010). For each fault, there is a larger magnitude (basically similar to USGS national maps) and a scenario with magnitude 7.0. The geometry and dimensions of these six scenarios are given in Table 2.

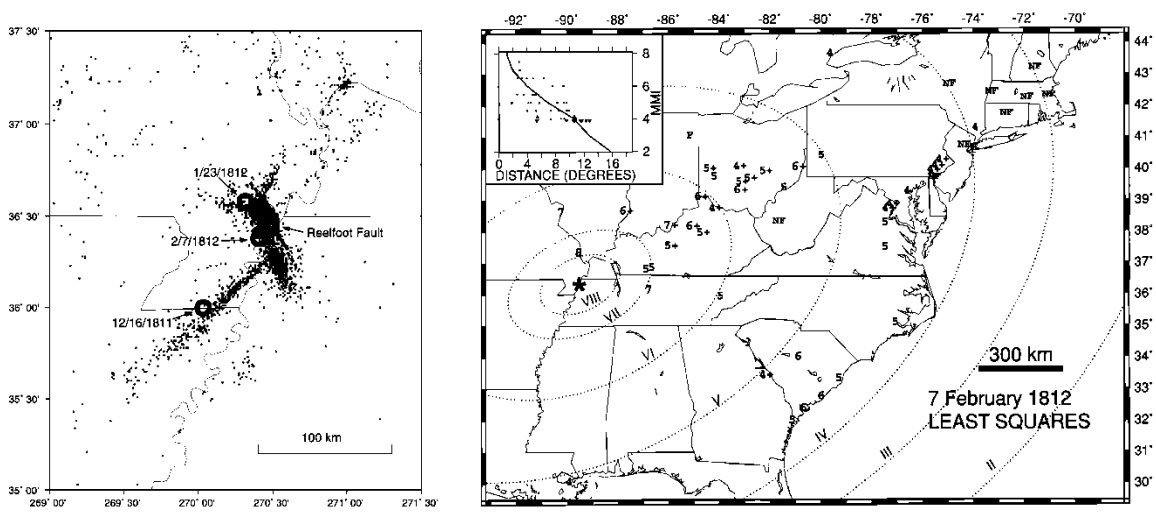

Figure 1: (Left) Map of the New Madrid region showing recent seismicity and inferred epicenter locations for the 1811 and 1812 earthquakes. (Right) Modified Mercalli intensities for the February 7, 1812 event based on reexamination of observed intensity reports. Source: Hough et al (2000).

The moment magnitude for each scenario is based on the magnitude-rupture area relation developed for stable continental regions by Leonard (2010). In addition, Somerville et al. (2001) derived the following relation for the average rise time on the fault,

$$Tr = 3.75 \times 10\text{-}9 * M_o^{1/3},$$

and they also found the high frequency stress parameter is 2.86 times larger, and the high frequency corner frequency scales by a factor of 0.5375 relative to values found for active tectonic regions.

Table 2. Fault parameters for 1811-1812 New Madrid scenarios.

Segment	Top center Lon.	Top center Lat.	Depth to top (km)	Length (km)	Width (km)	Strike	Dip	Rake (avg.)	M_w
Southwest	-90.0273	35.9036	0.0	140	22	229	90	180	7.7
	-89.8579	36.0230	4.0	60	11	229	90	180	7.0
Central	-89.3830	36.3386	0.0	60	40	162	38.7	90	7.6
	-89.4644	36.4356	3.0	30	22	162	38.7	90	7.0
Northeast	-89.4296	36.8260	0.0	70	22	207	90	180	7.4
	-89.5069	36.7036	1.0	40	15	207	90	180	7.0

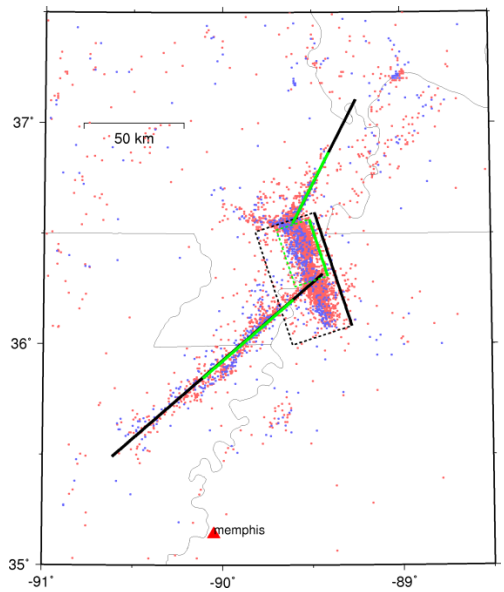

Figure 2. New Madrid region showing surface projection of six proposed fault segments for the 1811-1812 earthquakes. Black faults are larger magnitude scenarios, green faults are magnitude 7 scenarios. Background seismicity is shown in red (< 10 km depth) and purple (> 10 km depth) circles.

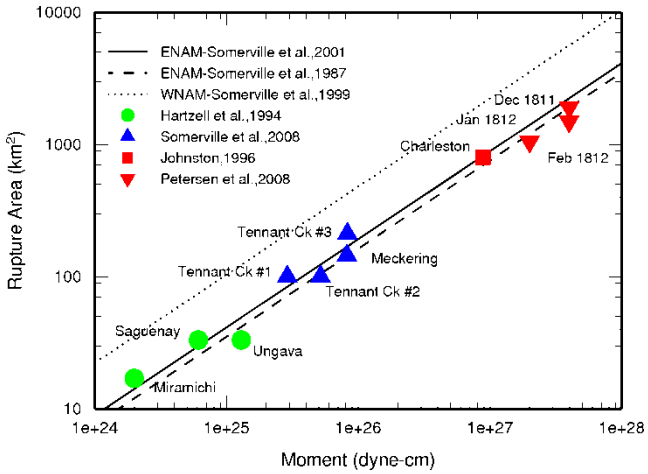

Figure 3: Seismic moment – rupture area scaling of ENA earthquakes and comparison with WNA earthquakes. Source: Modified from Somerville et al. (2001).

2.2 Rupture Models of 1811 and 1812 Earthquakes

Since little is known about the slip distribution and hypocenters for the 1811-1812 events, we ran a suite of scenarios to investigate the sensitivity of ground motions to these parameters. Based on past experience, the hypocenter can have a significant influence on the pattern and strength of ground motions, particularly at the lower frequencies (f < 1 Hz). For the larger magnitude scenarios, we ran 3 hypocenters for the Southwest segment (bilateral and 2 unilateral), and 2 hypocenters for the Central and Northeast segments (roughly 25% and 75% along strike). This provided 7 realizations. For the magnitude 7 scenarios, we also studied the case of a single hypocenter (bilateral) for the Southwest and Central segments. Therefore, we computed total 9 scenarios.

We generated a suite of kinematic rupture models for these 9 scenarios using the methodology of Graves and Pitarka (2010). Figure 4 shows three hypothetical scenarios for the Southwest segment (different slip distributions are created using different initial random number seeds). In addition to slip distribution, the Graves and Pitarka (2010) method prescribes the rupture initiation time and slip function at each point on the fault. The rise time varies with depth and the square root of local slip, with the average scaled to the Somerville relation. The average rupture speed is set to 80% of the local shear wave velocity, and also scales with depth and local slip amount. The rake is allowed to vary about the prescribed average. Figures 5 and 6 show hypothetical ruptures for the Mw 7.6 Central and Mw 7.4 Northeast segment scenarios. Figure 7 shows Mw 7 scenarios for the Southwest and Central segments.

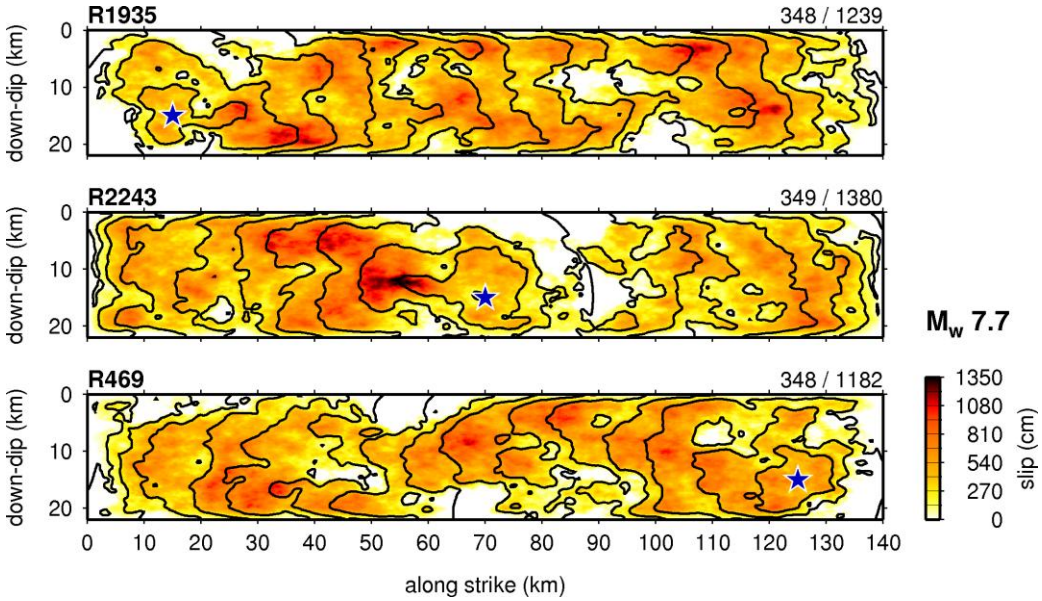

Figure 4. Three hypothetical rupture scenarios for the Mw 7.7 Southwest fault segment. Contours indicate rupture propagation time at 3 sec intervals.

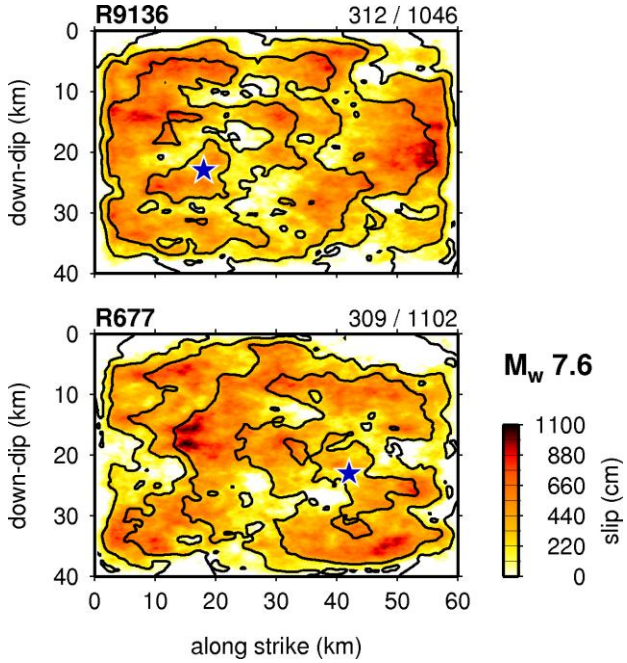

Figure 5. Two hypothetical rupture scenarios for the Mw 7.6 Central fault segment. Contours indicate rupture propagation time at 3 sec intervals.

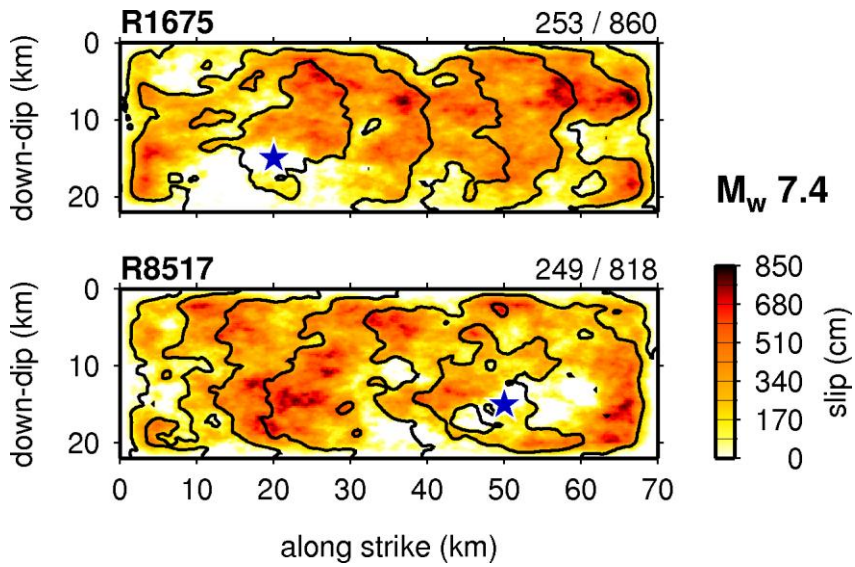

Figure 6. Two hypothetical rupture scenarios for the Mw 7.4 Northeast fault segment. Contours indicate rupture propagation time at 3 sec intervals.

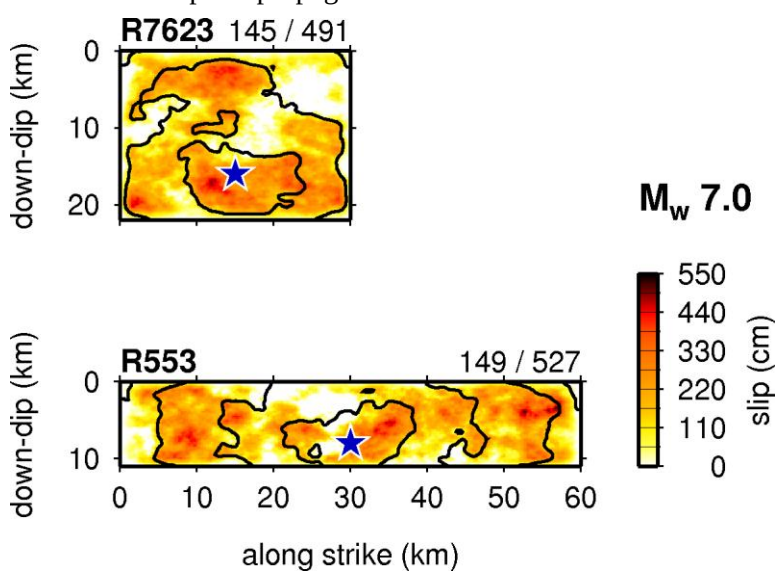

Figure 7. Two hypothetical M_w 7.0 rupture scenarios for the Southwest and Central fault segments. Contours indicate rupture propagation time at 3 sec intervals.

Figure 8A shows the target model region for our simulations. The primary region is a rectangular area 190 km by 360 km. We calculate broadband ground motions for each scenario on a 2 km by 2 km grid covering this region (17,100 sites). The simulations use the hybrid methodology of Graves and Pitarka (2010) with adjustments for stable continental regions as described in Somerville et al (2009). The 3D low frequency (f < 1 Hz) portion of the calculation uses a minimum shear wave velocity of 0.625 km/s and a grid spacing of 0.125 km. The high frequency (f > 1 Hz) calculation uses a generic 1D velocity profile with a Vs30 of 865 m/s. The Vs30 based site amplification factors used by Graves and Pitarka (2010) to generate site-specific ground motions were developed for active tectonic regions and may not be applicable to CEUS. The NGA-East program is currently investigating site response characteristics of CEUS and it is

expected that similar Vs30 based site amplification factors will eventually become available for this region.

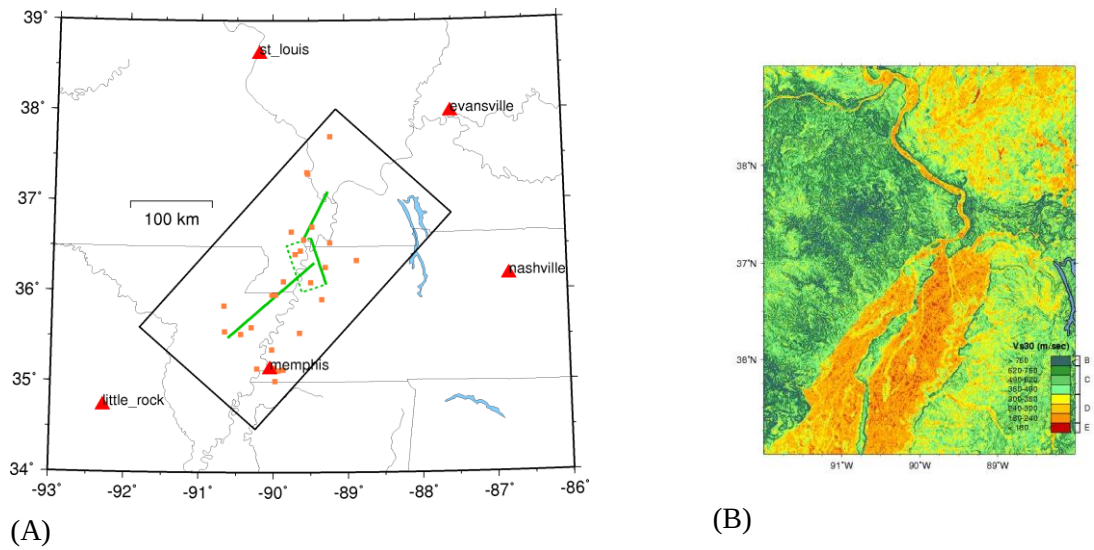

Figure 8. (A)Target model region for the broadband New Madrid scenario simulations. Green lines indicate the three (large magnitude) fault segments and the black rectangle is the 190 km by 360 km region covered by the 3DFD simulations. The orange squares are locations of recording sites. Additional 1D simulations may be done for the indicated cities. (B) Map of topography-based Vs30 for the New Madrid region, source: http://earthquake.usgs.gov/research/hazmaps/interactive/vs30.

3. Velocity Structure Model for New Madrid Region

In addition to source characterization, the specification of an appropriate crustal and near-surface velocity structure is vitally important for the ground motion simulation procedure. Our simulation approach utilizes site-specific Vs30 (travel time average shear wave velocity in the upper 30 meters) values to develop appropriate amplification factors (procedure discussed in more detail later). While this approach is less sophisticated than more detailed site response analysis (e.g. Toro and Silva, 2001; Cramer, 2006), it is extremely cost effective to implement and allows us to generate detailed maps of ground response on a large scale. Furthermore, the USGS has recently made available a tool to extract Vs30 values for any region of the US (http://earthquake.usgs.gov/research/hazmaps/interactive/vs30). These maps are generated using the Vs30/topography relation described in Wald and Allen (2007). Figure 8B shows a pre-generated grid of Vs30 values for the New Madrid region obtained from the above website.

Previous studies have proposed various models of crustal velocity structures in the CEUS. The recent work by Saikia et al (2006) developed a comprehensive crustal velocity model for the New Madrid region and considered the effects of 2D and 3D structure on the ground motion response. Recently a 3D community velocity model (CUSVM1.2) of CEUS was made available (Ramirez-Guzman et al., 2010). The model is based on multiple data sets

including seismic refraction and reflection lines, geophysical logs, and inversions of the regional seismic properties, and is the most updated and well accepted 3D model for CEUS. Therefore, we adopt this model for ground motion simulation, and validate its accuracy with recorded ground motion from the April 18th, 2008 M5 Mt Carmel earthquake.

4 Simulations for Specified Scenario Earthquakes

4.1 The hybrid broadband ground motion simulation methodology

The method that we will use to simulate broadband ground motions of these earthquakes is a hybrid procedure that combines a stochastic approach at high frequencies and a deterministic approach at low frequencies. A detailed description of this methodology is given in Graves and Pitarka (2004), which we briefly summarize below.

Deterministic Methodology (f < 1 Hz)

At low frequencies, we use a deterministic representation of source and wave propagation effects. The basic calculation is carried out using a 3D viscoelastic finite-difference algorithm, which incorporates both complex source rupture as well as wave propagation effects within arbitrarily heterogeneous 3D geologic structure (Graves, 1996; Pitarka, 1999). Anelasticity is incorporated using the coarse-grain approach of Day and Bradley (2001). We use a kinematic description of fault rupture, incorporating spatial heterogeneity in slip and rupture velocity by dividing the fault into a number of subfaults. We use a slip velocity function that is constructed using two triangles following from the dynamic rupture analysis of Guaterri et al. (2003). The rise time comes from the empirical analysis of Somerville et al. (1999) who find that CEUS events have average rise time that are 1.85 times longer than events in tectonically active regions. The rupture initiation time (T_i) is determined using the expression

$$T_i = R / V_r - \delta t \tag{1}$$

where R is the rupture path length, V_r is the background rupture velocity (set at 80% of V_s), and δt is a timing perturbation that scales linearly with slip amplitude such that $\delta t = \delta t_0$ where the slip is at its maximum and $\delta t = 0$ where the slip is at the average slip value. We set $\delta t_0 = 0.5\text{sec}$. This scaling results in faster rupture across portions of the fault having large slip as suggested by source inversions of past earthquakes (Yaji, 2004) and dynamic rupture models (Day, 1982). For scenario earthquakes, the slip distribution can be specified using randomized spatial fields, constrained to fit certain wave number properties (e.g., Somerville et al., 1999; Mai and Beroza, 2002). An example of a rupture model constructed using the above approach is shown below in Figure 10.

High Frequency Methodology (f > 1 Hz)

The high frequency portion of the simulation methodology has its roots in the pioneering work of Brune (1970) and Hanks and McGuire (1981) with the formal simulation approach for point sources first developed by Boore (1983) and the extension to finite-faults given by Frankel (1995), Beresnev and Atkinson (1997) and Hartzell et al. (1999). Recent work by Atkinson et al (2009) and Boore (2009) provide systematic comparisons of the point-source and finite-fault stochastic formulations. In our approach, the fault is divided into a number of

subfaults and we sum the response for each subfault assuming a random (stochastic) phase, a wavenumber-squared source spectrum, and simplified Green's functions calculated for a specified 1D velocity structure.

A basic premise of this approach is that it is designed to utilize the random phasing of the radiated subfault waveform to represent the poorly constrained and/or unknown details of the rupture process. For this reason, we choose to limit the subfault size used for the high frequency calculation to have a minimum characteristic dimension no smaller than about 1 km. Using smaller subfaults deteriorates the fidelity of the approach because as the number of subfaults used in the summation increases, the solution can become deficient for certain frequencies due to destructive interference of the random phasing (e.g., Joyner and Boore, 1986). The exact nature of these deficiencies and their frequency extent will depend on the specified rupture, the specified velocity structure, and the locations of the observation sites. While the specific choice of a minimum 1 km limit on subfault size is somewhat arbitrary, we have found this approach produces credible results, as will be demonstrated later by example.

In our approach, each subfault ($i=1,N$) contributes an acceleration amplitude spectrum given by

$$A_i(f) = \sum_{j=1,M} C_{ij} S_i(f) G_{ij}(f) P(f) \qquad (2)$$

where $\omega=2\pi f$ is the angular frequency and the summation over $j=1,M$ accounts for different rays (e.g., direct, Moho-reflected). The radiation scale factor C_{ij} is given by

$$C_{ij} = \frac{F_s R_{Pij}}{4\pi\rho_i \beta_i^3} \qquad (3)$$

where $F_s=2$ accounts for free surface amplification, R_{Pij} is a conically averaged radiation pattern term spanning a range of +/- 45 degrees in slip mechanism and take-off angle, and ρ_i and β_i are the density and shear wave velocity at the center of the subfault. The source radiation spectrum is given by

$$S_i(f) = m_i F f^2 \left[1 + F\left(f/f_{ci}\right)^2\right]^{-1} \qquad (4)$$

where $m_i = d_i \mu_i A_T / M_o$ is the relative seismic moment of the ith subfault and $F = M_o/(N\sigma_p dl^3)$ is a factor introduced by Frankel (1995), which scales the subfault corner frequency to that of the mainshock and ensures the total moment of the summed subfaults is the same as the mainshock moment (M_o). The slip and rigidity of the ith subfault are given by d_i and μ_i, respectively, A_T is the total fault area, N is the total number of subfaults, σ_p is the Brune stress parameter (set 50 bars for WUS, and 143 bars for CEUS), and dl is the average subfault dimension. The subfault corner frequency is given by

$$f_{ci} = \frac{c_0 V_{Ri}}{\alpha_\tau \pi dl} \qquad (5)$$

where c_0 is an empirically determined constant., and it is chosen to be 2.1 for WUS by default. But for the CEUS, it is scaled by 1/1.85 to get c0=1.13 for CEUS simulations, to account for difference in rise time for WUS and CEUS.

V_{Ri} is the local rupture speed at the subfault as given by equation (4) and α_τ is the dip related scale factor given by equation (9).

The path term is given by

$$G_{ij}(f) = \frac{I_i(f)}{r_{ij}} \exp\left[-\pi f^{1-x} \sum_{k=1,L} t_{ijk} / q_k \right] \quad (6)$$

where r_{ij} is the total path length of the jth ray from the ith subfault to the receiver and $I_i(f)$ represents gross impedance effects calculated using quarter wavelength theory (Boore and Joyner, 1997) within the specified 1D velocity structure. Anelasticity is incorporated via a travel-time weighted average of the Q values for each of the velocity layers (Ou and Herrmann, 1990) with an assumed frequency dependence of the form $Q(f)=Q_o f^{x}$. The summation over $k=1,L$ represents all of the ray path segments through the layers of the 1D velocity model, with t_{ijk} and q_k being the travel time of the particular ray segment and Q value, respectively, within each velocity layer k. The constant Q of each velocity layer is modeled as a linear function of the shear wave velocity

$$q_k = a + b\beta_k \quad (7)$$

with the constants a and b determined empirically. For CEUS, high frequency Q is scaled by 4 relative to WUS, that is Q = 160 + 34 * Vs (Atkinson & Beresnev, 1999 & 2002). As compared to the Q model by Hartzell and Mendoza (2011), our Q is a little bit smaller. Finally, the high frequency spectral decay is modeled as, (Anderson and Hough, 1984).

$$P(f) = \exp(-\pi\kappa f) \quad (8)$$

For CEUS, Kappa (κ) is set to be 0.005 outside the Mississippi Embayment and 0.02 within the Embayment (Campbell, 2009).

Following the method of Boore (1983), the phase spectrum of the radiated acceleration for each ray is derived from a windowed time sequence of band-limited white Gaussian noise. We use a Saragoni and Hart (1974) windowing function with the peak of the envelop set at the direct S-wave arrival time with ε=0.2 and η=0.05 (see Boore, 1983, p. 1869). The duration of the window for the ith subfault is given by

$$T_{di} = f_{ci}^{-1} + c_1 R_i \quad (9)$$

where $c_1 = 0.063$ is an empirically determined constant and R_i is the horizontal distance from the ith subfault to the receiver.

Site Specific Amplification Factors

In order to account for site specific geologic conditions in the final broadband response, we apply period-dependent, non-linear amplification factors to the simulated time histories. These factors are based on the 30 m travel-time averaged shear wave speed (V_s^{30}) at the site of interest. Both the long period (3-D) and short period (1-D) computational models have minimum V_s^{30} values truncated at a constant reference value, typically between 600 m/s and 1000 m/s. This is done not only for computational efficiency, but also reflects our lack of sufficient knowledge regarding the detailed nature of the subsurface velocity structure, particularly in the upper few hundred meters. The site-specific amplification factors are based on equivalent-linear site response analysis (Walling et al., 2008) as implemented in the GMPE of Campbell and Bozorgnia (2008). Those theoretical site factors have been shown to be generally consistent with empirical observation (Kwok and Stewart, 2006). These site factors have the general form

$$F(T_i) = f(v_{site}, pga_R, T_i) / f(v_{ref}, pga_R, T_i) \quad (4)$$

where T_i are the discrete periods given by Campbell and Bozorgnia (2008), $f(x,y,z)$ is a function containing period-dependent coefficients, v_{site} denotes V_s^{30} at the site of interest, v_{ref} corresponds to the V_s^{30} used in the simulation, and pga_R denotes the rock level PGA from the short period calculation. We construct smoothly varying functions by linearly interpolating between the factors at the discrete periods and then apply these to the Fourier amplitude spectra of the simulated responses. For the Vs30 site model, we adopt a simple model of Vs30 site featuring Vs30=625 m/s for embayment sites and Vs30=1100m/s for non-embayment sites. Finally, we combine the individual stochastic and deterministic responses into a single broadband time history using a set of matched Butterworth filters (Hartzell et al., 1999).

The broadband ground motion simulation procedure described above has been applied to model the recordings of a number of earthquakes, including the 1979 Imperial Valley, 1989 Loma Prieta, 1992 Landers, 1994 Northridge, 1995 Kobe, 1999 Izmit, and 1999 Chi-Chi events (Graves and Pitarka, 2004; Graves, 2004). The simulation methodology reproduces the observed ground motions over the period range 0.1 to 10 seconds without any systematic bias, and with a sigma of about 0.5. In addition, the methodology is able to reproduce key ground motion features such as basin response, rupture directivity, footwall/hanging wall effects, and differences between shallow and buried rupture. It has been demonstrated that there is no systematic bias in the simulation of these data, which span magnitudes from 6.6 to 7.4 and include both buried and surface rupturing events. This indicates that the scaling of slip velocity with rupture depth that is used in the simulation procedure accurately reproduces the trends seen in the observations.

4.2 Validation of the methodology and velocity model with the 2008 Mt. Carmel earthquake.

In order to validate the hybrid broadband ground motion simulation method and the 3D velocity model, we compare synthetic ground motion with observation for the April 18th, 2008 Mt Carmel, Illinois earthquake, which is the strongest and the best recorded event in the past decade near the New Madrid region. Both long period (>5s) and high frequency signals from this event (>2Hz) show high signal noise ratio for distances up to 500km.

In order to achieve accurate ground motion simulation, first we need the source parameters of the earthquake. We refined the source parameters of these earthquakes with a different algorithm than that of Herrmann et al. (2008). The source inversion is performed with the Cut and Paste method (CAP) (Zhu and Helmberger, 1996). In this algorithm, full waveforms are cut into the Pnl segment and the S+surface wave segment. Each segment is fit with synthetic seismograms separately. The CAP algorithm is basically a grid search inversion with synthetic seismograms calculated for a 1D layered crustal model appropriate for the area, with time shifting of the Pnl and surface wave parts to allow for inaccuracy in the velocity model (Zhu and Helmberger, 1996). Moreover, the amplitude of the waveforms is also adjusted according to their distances in order to suppress overweighting of close stations, thus leading to a much more balanced inversion of the source mechanism. Focal depth can also be well resolved because the Pnl waveform is sensitive to focal depth and the amplitude ratio between the surface wave and the Pnl wave provides good constraints on focal depth. The derived source parameters are shown in Figure 9, and are consistent with the moment obtained with the approach of Empirical Green's Function (Hartzell and Mendoza, 2011).

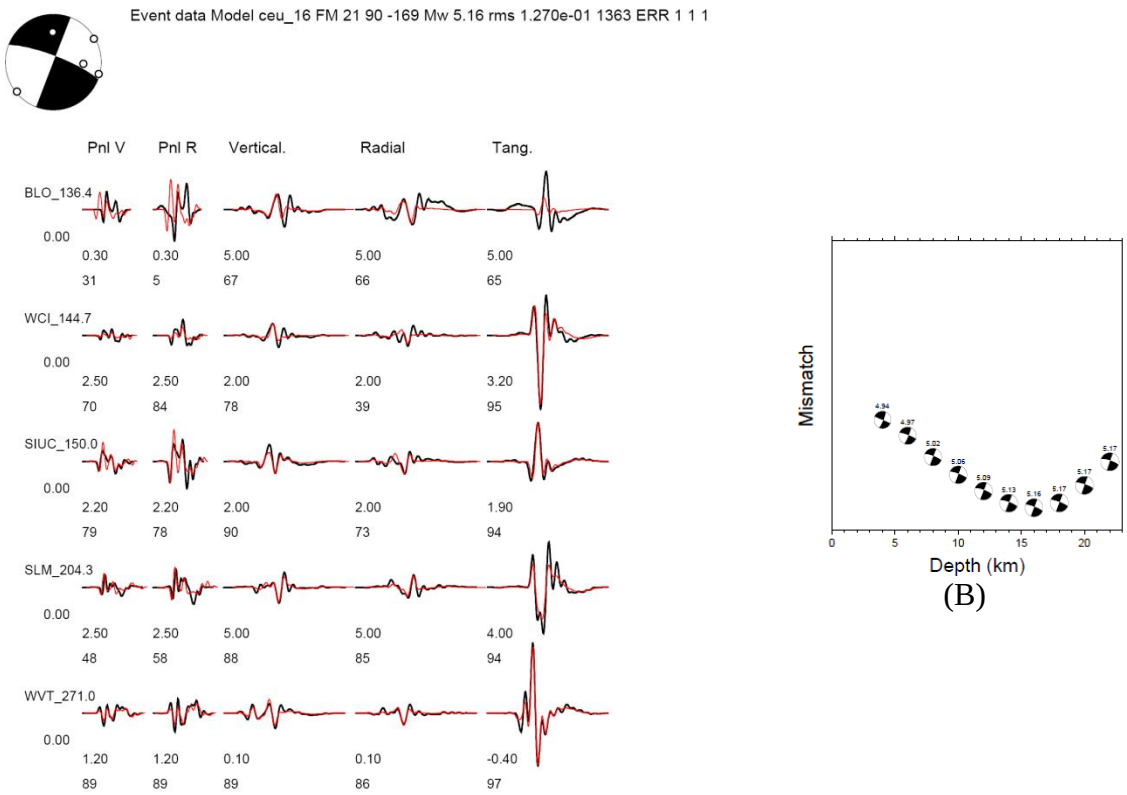

Figure 9 (A),"Cut and Paste" (CAP) modeling of the Pnl and Surface waves for the Mt. Carmel event.. (B) Depth sensitivity from CAP inversion of the Mt Carmel event. The optimal estimate of depth is 16 km, close to that obtained by Herrmann et al (2008).

With point source parameters of the Mt Carmel earthquake resolved, we generate a finite fault model for the event with randomized rake angle, rise time and slip (Figure 10), whose distribution follows a k^{-2} law in the wave number domain, and the summed moment is constrained to conserve the point source moment tensor solutions. For low frequency (f < 0.5Hz), synthetic ground motions fit the observation well (Figure 11), suggesting that the 3D model and the rupture model work well.

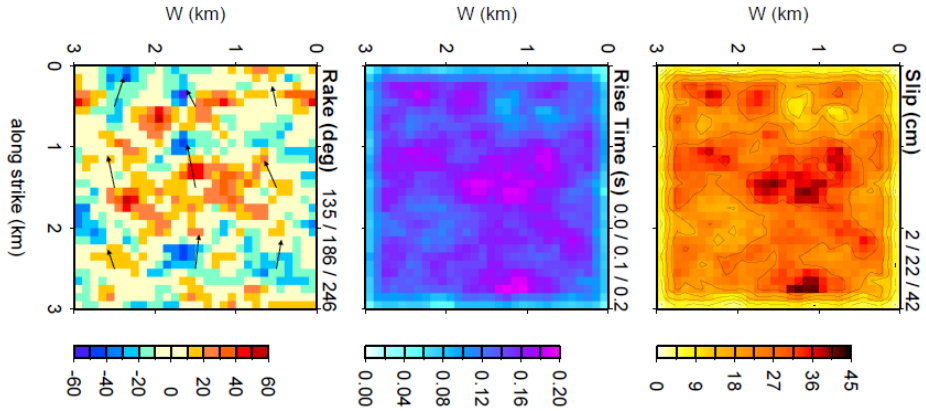

Figure 10. A finite fault model of rake angle (left), rise time (middle) and slip for the Mt Carmel event.

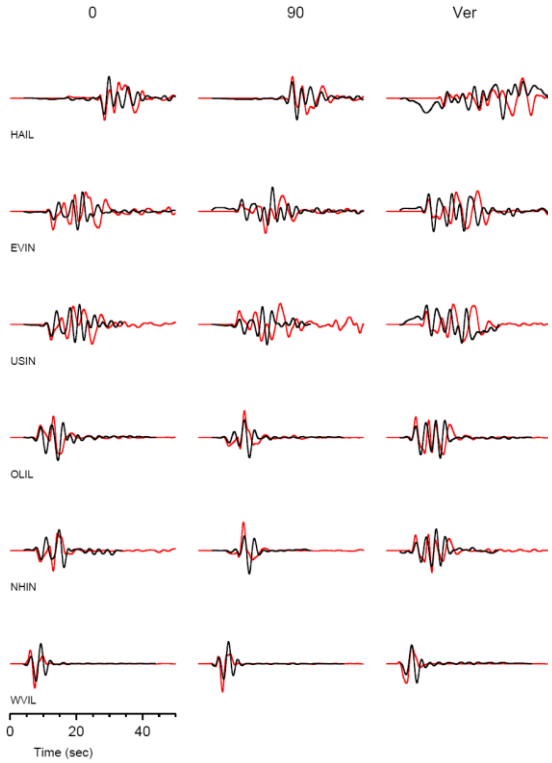

Figure 11. Comparison between observed (black) and synthetic (red) ground motion for the Mt. Carmel earthquake. Seismograms are ground velocities low-pass filtered with $f < 0.5$ Hz.

5 **Develop Maps of Simulated Ground Motion**

After the 3D velocity model and the broadband ground motion simulation method validated with the Mt. Carmel earthquake data, we proceed to compute ground motion for the 9 scenarios. The results are presented as various maps in Figures 13-21. In these figures, spectral acceleration (SA) at period 3.0 second, 1.0 second and 0.3 second for horizontal component 1 (H1, parallel to the north-east orientation of the rectangle in Figure 8) and horizontal component 2 (H2, parallel to the north-west orientation), PGA, PGV, and H1 and H2 of PGA and PGV, as well as instrumental intensity (MMI) (i.e., ShakeMaps) are plotted.

In order to get insight into which combinations of hypocenter location and rupture velocity are most consistent with the observed shaking patterns and levels, we need to remove the baseline trend of the ground motion. For each ground motion measure (SA, PGV, PGA, MMI), we use the ground motion attenuation relation proposed by Somerville et al. (2001) to fit data points as extracted from these simulation results. In Figure 12, it is clear that the simulated ground motions (black) are well fitted by the form of the attenuation relations (red) based on 1D simulations (Somerville et al., 2011), which is one of the models used in the generation of the USGS National Seismic Hazard Maps. After the baseline trend is removed, substantial scatter is observed for longer period (3.0 seconds) ground motions, but not for high frequency (0.3 seconds) ground motions.

As expected, the lateral variation of ground motion is much more obvious on maps of various ground motion parameters after the baseline trend is removed (right column for all panels in Figures 13-21). For all the unilateral rupture scenarios, the directivity effect (on PGA, PGV and SA) is clear, with ground motion in the forward rupture direction stronger, and weaker in the backward rupture direction. For long period motion (>3sec), basin effects are seen as the Mississippi embayment typically amplifies ground motion substantially, but for short period ground motions, basin effect is not obvious. Therefore, PGV shows obvious basin effects, but PGA does not show substantial basin effects. When rupture propagates towards the embayment from the events on the northeastern fault, rupture directivity effects and basin effects combine to produce very strong motions in the embayment. Therefore, intensity observations could have overestimated the magnitude in this case.

Moreover, PGV, PGA, and Intensity all seem to be symmetric about the fault, but their H1, H2 components are not necessarily symmetric about the fault. For example, in Figure 14 (the top rupture model in Figure 4, for the southwest fault), the H2 component of PGV is stronger to the east of the fault along rupture direction, but the H1 component of PGV is higher to the west of the fault. For instrumental intensity, the ground motion is a combination of both H1 and H2 components, and the asymmetry effect is reduced by averaging these two components.

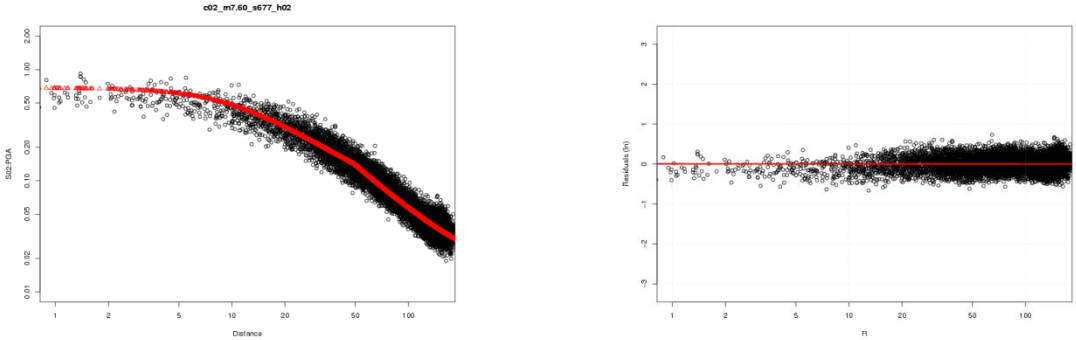

A

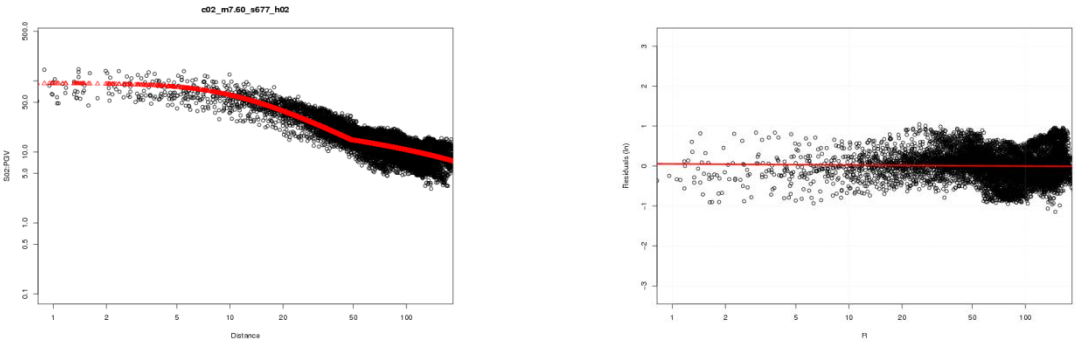

B

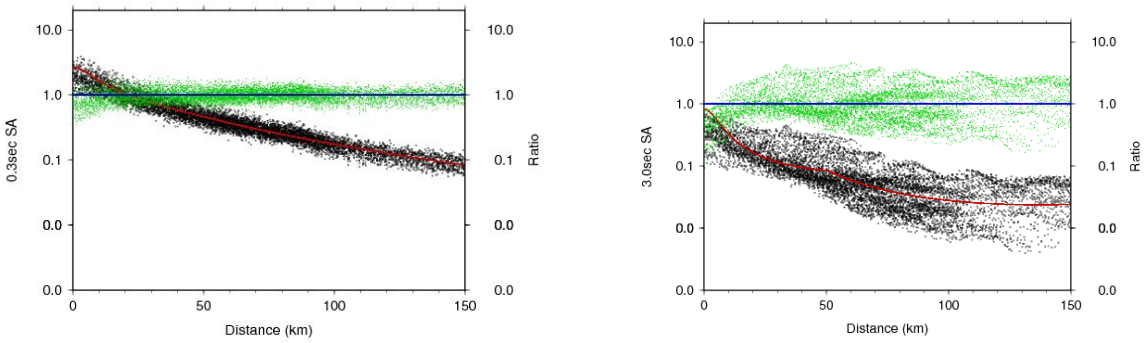

C

Figure 12, (A) left, Observed (black circles) PGA vs distance and fitted baseline trend (red line). Right, Ratio of observed PGA and the baseline value for given distance, and it is plotted in log-scale. (B) same as (A), but PGV is plotted. (C) Left, Observed (black dots) Spectral Acceleration at period of 0.3 sec, its baseline trend fit (red line) and Spectral Acceleration after baseline trend removed. Right: same as left, but for a period of 3.0 seconds.

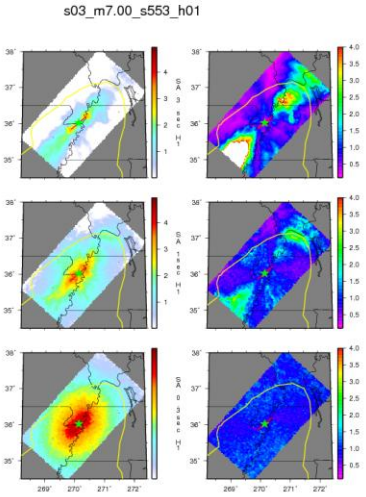

A

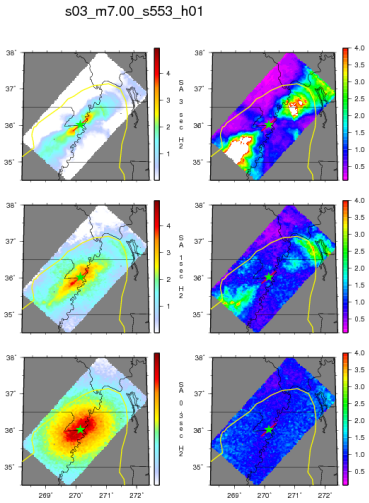

B

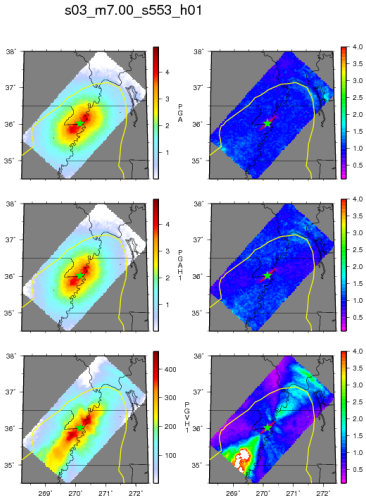

C

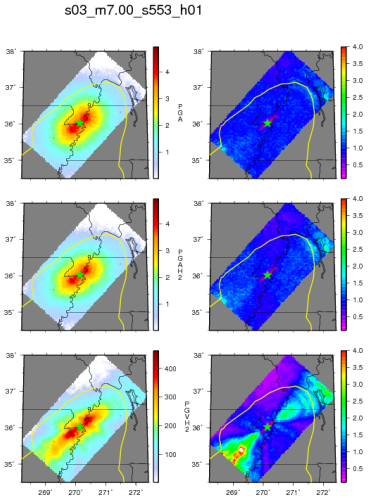

D

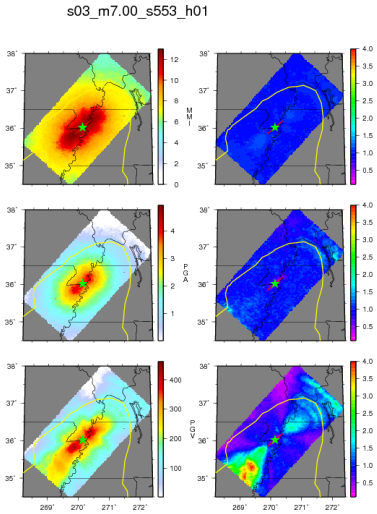

E

Figure 13. Simulated ground motion for rupture model S553, southwest fault. Mw is 7.0. For each panel the left column is map of simulated ground motion, and the right column is ground motion after base line trend removed. (A) H1 component of SA at period 3.0sec (top), 1.0 sec (middle) and 0.3 sec (bottom) (B) H2 component of SA at period 3.0sec (top), 1.0 sec (middle) and 0.3 sec (bottom) (C) PGA (top), H1 component of PGA (middle), H1 component of PGV (bottom) (D) PGA (top) H2 component of PGA (middle), H2 component of PGV (bottom). (E) Instrument Intensity (top), PGA (middle) and PGV (bottom).

The basin effect is particularly strong for PGV. Rupture directivity effects are also observed, with larger ground motions along the fault away from the epicenter.

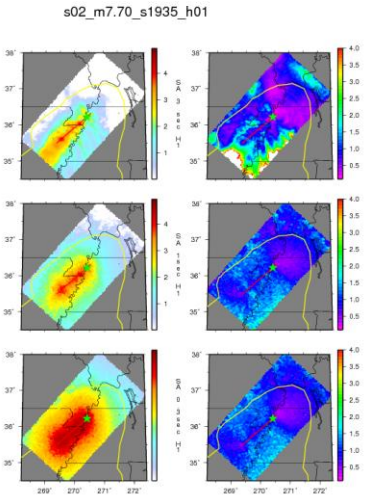

A

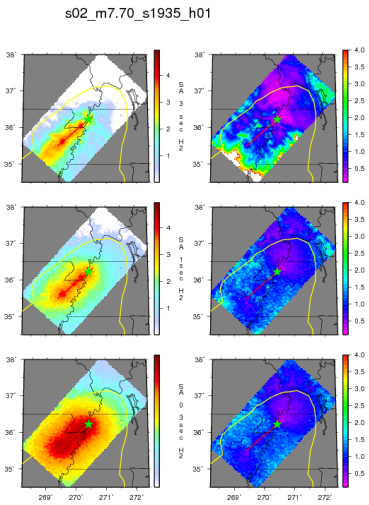

B

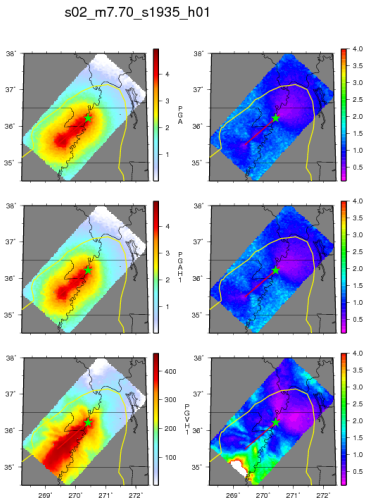

C

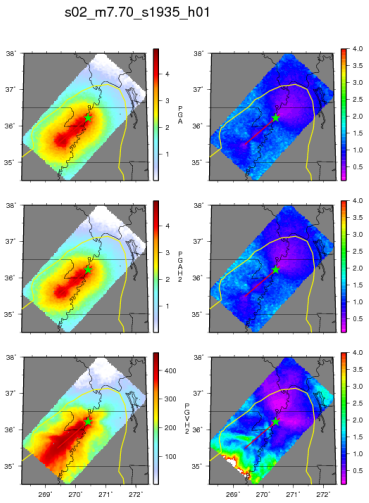

D

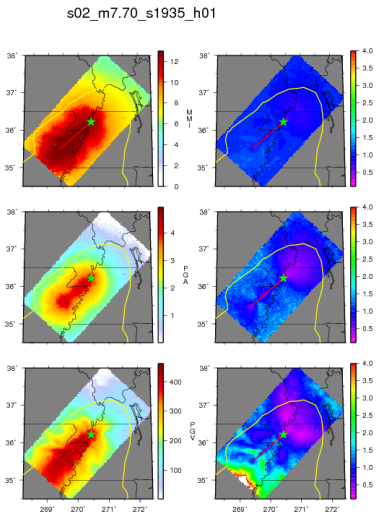

E

Figure 14. Simulated ground motion for rupture model S1935, southwest fault. Mw is 7.7. For each panel the left column is map of simulated ground motion, and the right column is ground motion after base line trend removed. (A) H1 component of SA at period 3.0sec (top), 1.0 sec (middle) and 0.3 sec (bottom) (B) H2 component of SA at period 3.0sec (top), 1.0 sec (middle) and 0.3 sec (bottom) (C) PGA (top), H1 component of PGA (middle), H1 component of PGV (bottom) (D) PGA (top) H2 component of PGA (middle), H2 component of PGV (bottom). (E) Instrument Intensity (top), PGA (middle) and PGV (bottom).

The basin effect is particularly strong for PGV. Rupture directivity effects are also very strong, with ground motion to the southwest much stronger than to the northeast.

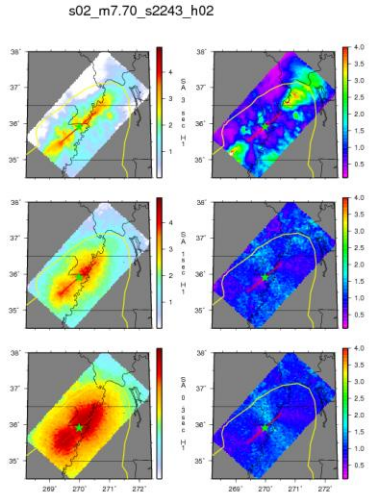

A

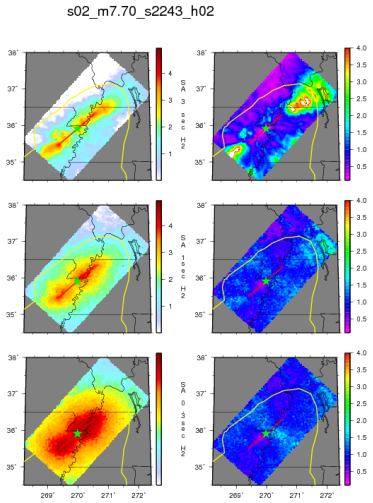

B

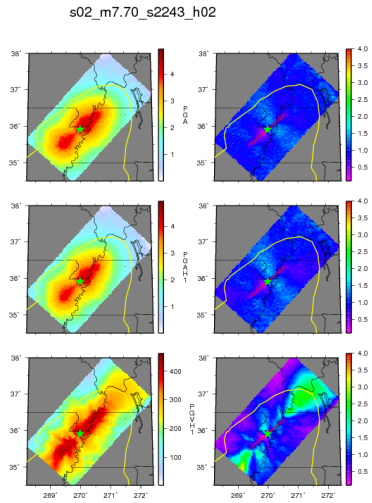

C

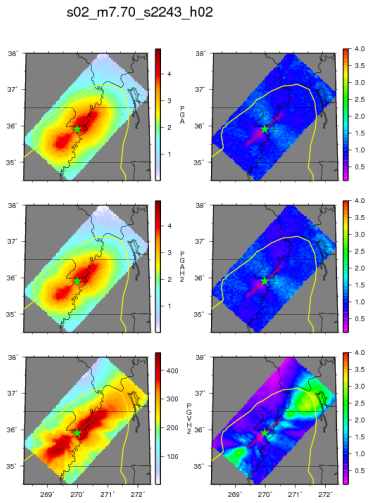

D

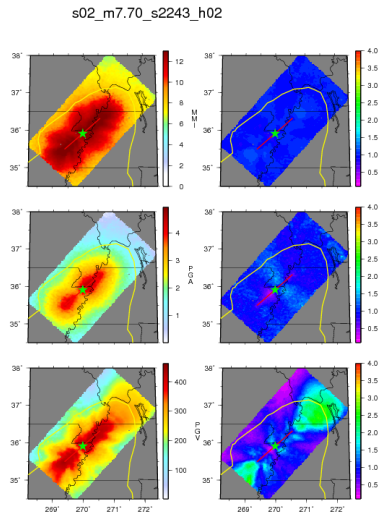

E

Figure 15. Simulated ground motion for rupture model S2243,southwest fault. Mw is 7.7. For each panel the left column is map of simulated ground motion, and the right column is ground motion after base line trend removed. (A)H1 component of SA at period 3.0sec (top), 1.0 sec (middle) and 0.3 sec (bottom) (B) H2 component of SA at period 3.0sec (top), 1.0 sec (middle) and 0.3 sec (bottom) (C) PGA (top), H1 component of PGA (middle), H1 component of PGV (bottom) (D) PGA (top) H2 component of PGA (middle), H2 component of PGV (bottom). (E) Instrument Intensity (top), PGA (middle) and PGV (bottom).

Rupture directivity effects are observed for PGV, with large ground motions along fault away from the epicenter. PGA has large ground motions in a band perpendicular to the fault.

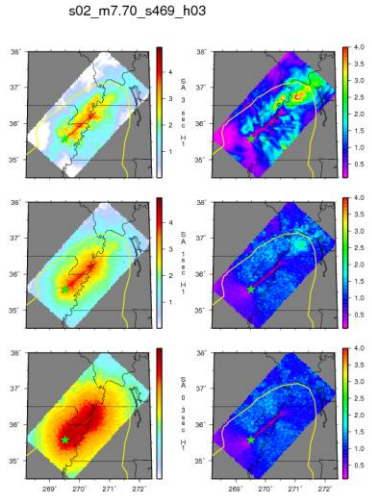

A

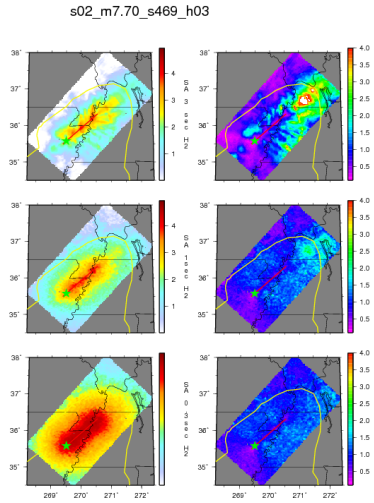

B

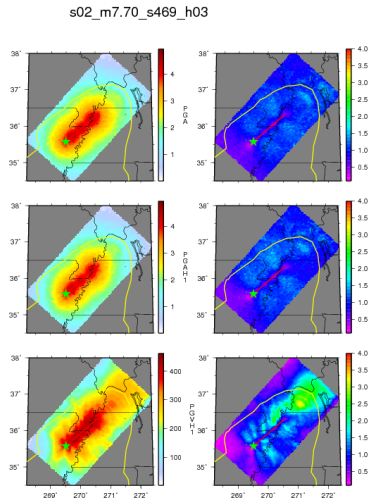

C

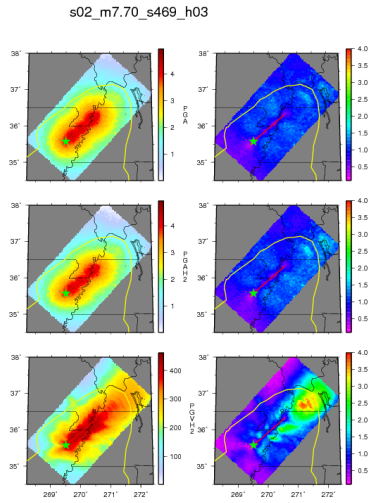

D

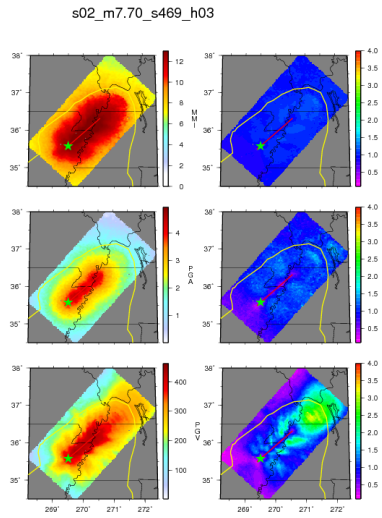

E

Figure 16. Simulated ground motion for rupture model S469, southwest fault. Mw is 7.7. For each panel the left column is map of simulated ground motion, and the right column is ground motion after base line trend removed. (A)H1 component of SA at period 3.0sec (top), 1.0 sec (middle) and 0.3 sec (bottom) (B) H2 component of SA at period 3.0sec (top), 1.0 sec (middle) and 0.3 sec (bottom) (C) PGA (top), H1 component of PGA (middle), H1 component of PGV (bottom) (D) PGA (top) H2 component of PGA (middle), H2 component of PGV (bottom). (E) Instrument Intensity (top), PGA (middle) and PGV (bottom).

Rutpure directivity effects are observed, with much stronger ground motions to the northeast. Basin effects are not obvious, probably because rupture is beneath the deepest part of the embayment.

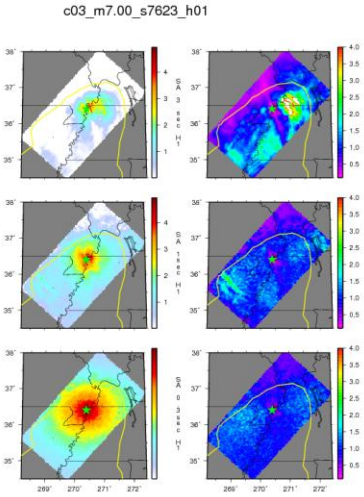

A

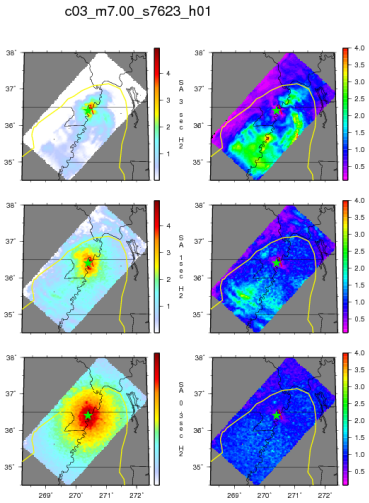

B

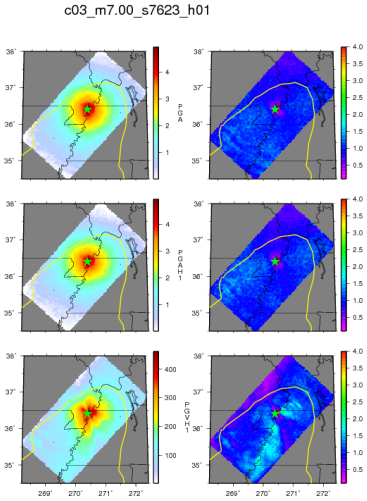

C

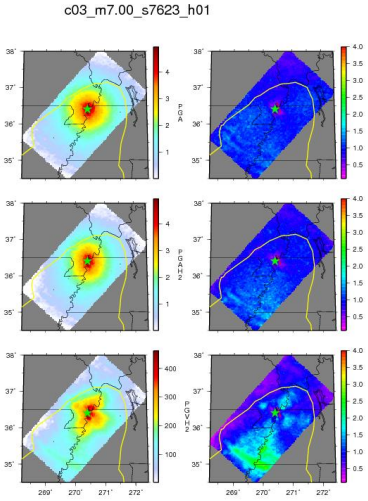

D

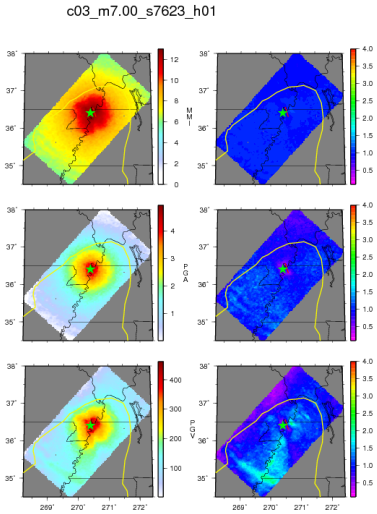

E

Figure 17. Simulated ground motion for rupture model S7632, central fault. Mw is 7.0. For each panel the left column is map of simulated ground motion, and the right column is ground motion after base line trend removed. (A)H1 component of SA at period 3.0sec (top), 1.0 sec (middle) and 0.3 sec (bottom) (B) H2 component of SA at period 3.0sec (top), 1.0 sec (middle) and 0.3 sec (bottom) (C) PGA (top), H1 component of PGA (middle), H1 component of PGV (bottom) (D) PGA (top) H2 component of PGA (middle), H2 component of PGV (bottom). (E) Instrument Intensity (top), PGA (middle) and PGV (bottom).
Basin effects are large for PGV.

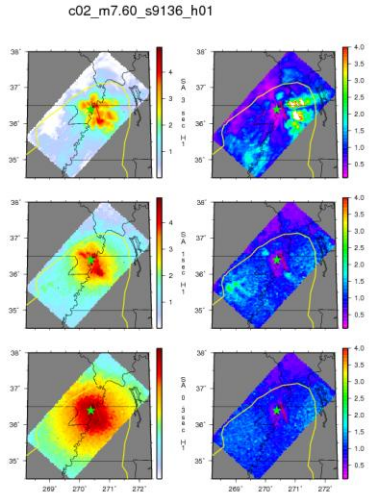

A

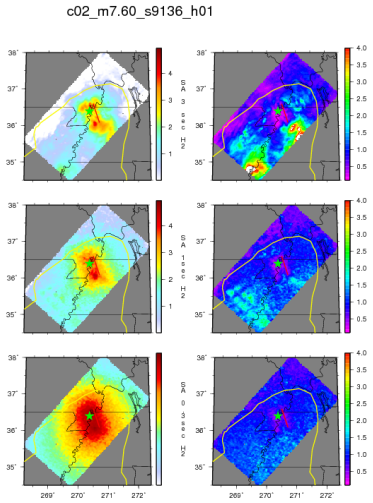

B

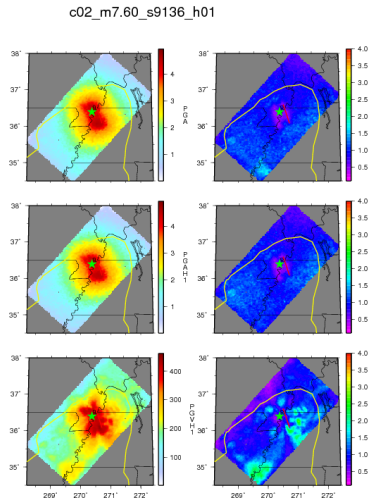

C

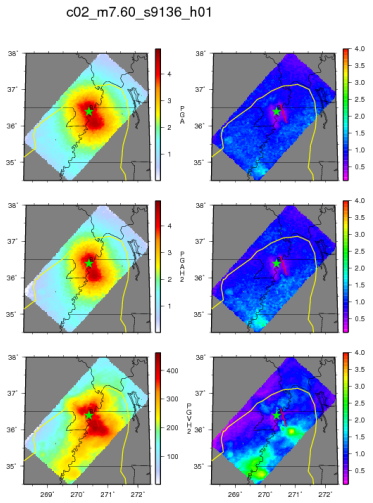

D

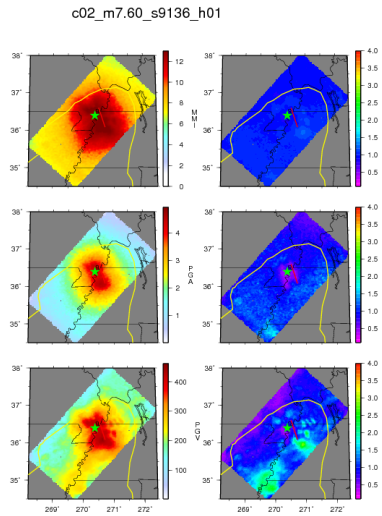

E

Figure 18. Simulated ground motion for rupture model S9136, central fault. Mw is 7.60. For each panel the left column is map of simulated ground motion, and the right column is ground motion after base line trend removed. (A)H1 component of SA at period 3.0sec (top), 1.0 sec (middle) and 0.3 sec (bottom) (B) H2 component of SA at period 3.0sec (top), 1.0 sec (middle) and 0.3 sec (bottom) (C) PGA (top), H1 component of PGA (middle), H1 component of PGV (bottom) (D) PGA (top) H2 component of PGA (middle), H2 component of PGV (bottom). (E) Instrument Intensity (top), PGA (middle) and PGV (bottom).

Both basin effects and directivity effects are evident.

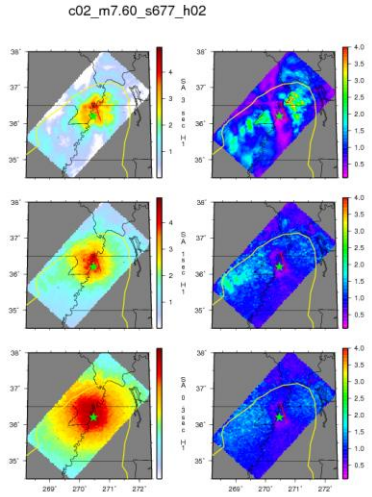

A

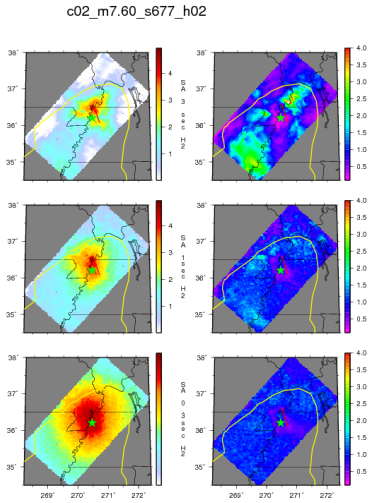

B

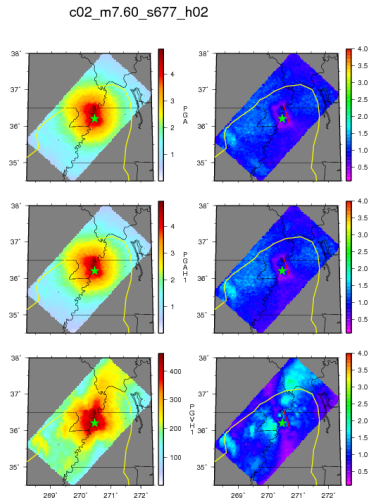

C

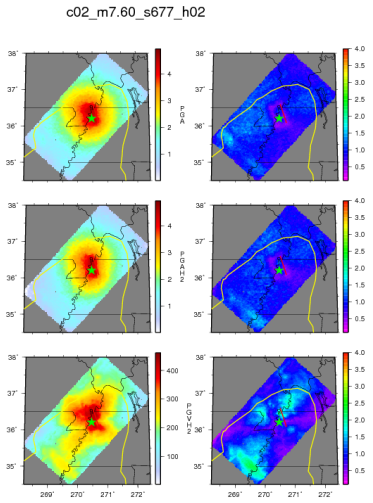

D

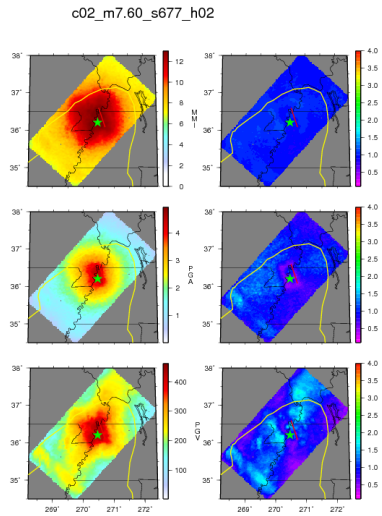

E

Figure 19. Simulated ground motion for rupture model S677, central fault. Mw is 7.6. For each panel the left column is map of simulated ground motion, and the right column is ground motion after base line trend removed. (A)H1 component of SA at period 3.0sec (top), 1.0 sec (middle) and 0.3 sec (bottom) (B) H2 component of SA at period 3.0sec (top), 1.0 sec (middle) and 0.3 sec (bottom) (C) PGA (top), H1 component of PGA (middle), H1 component of PGV (bottom) (D) PGA (top) H2 component of PGA (middle), H2 component of PGV (bottom). (E) Instrument Intensity (top), PGA (middle) and PGV (bottom).
Directivity effects are strong for PGV, and basin effects are also present.

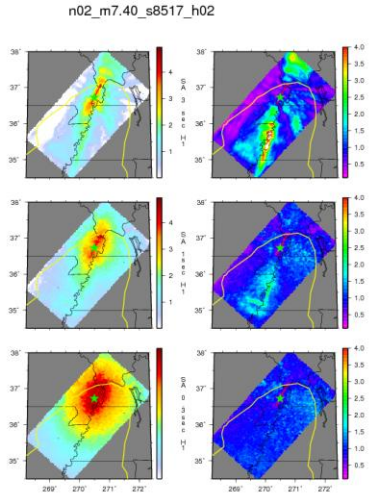

A

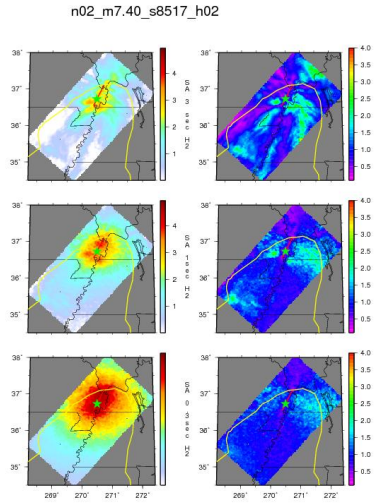

B

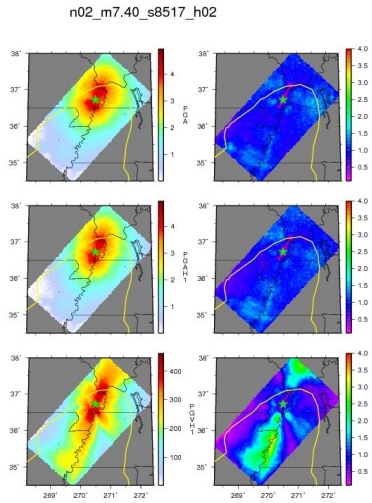

C

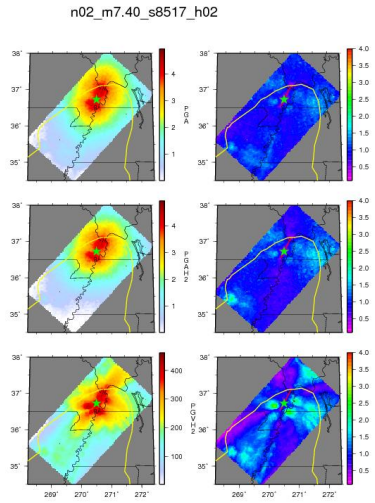

D

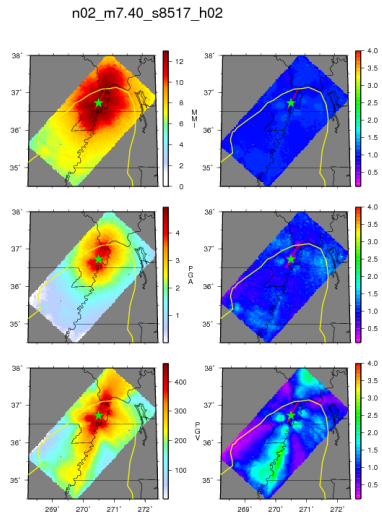

E

Figure 20. Simulated ground motion for rupture model S8517, northeasten fault. Mw is 7.4. For each panel the left column is map of simulated ground motion, and the right column is ground motion after base line trend removed. (A)H1 component of SA at period 3.0sec (top), 1.0 sec (middle) and 0.3 sec (bottom) (B) H2 component of SA at period 3.0sec (top), 1.0 sec (middle) and 0.3 sec (bottom) (C) PGA (top), H1 component of PGA (middle), H1 component of PGV (bottom) (D) PGA (top) H2 component of PGA (middle), H2 component of PGV (bottom). (E) Instrument Intensity (top), PGA (middle) and PGV (bottom).

Basin effects are strong for PGV, because the source is located outside of the basin. Rupture directivity effects are also obvious for PGV. PGA is strong in a band perpendicular to the fault.

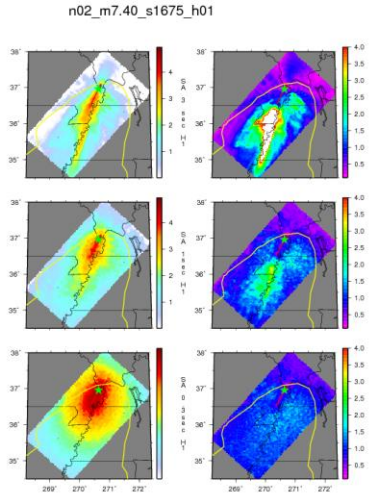

A

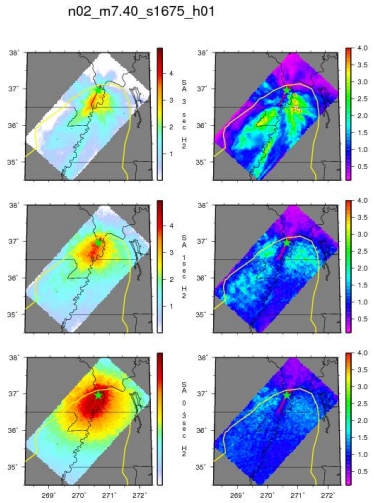

B

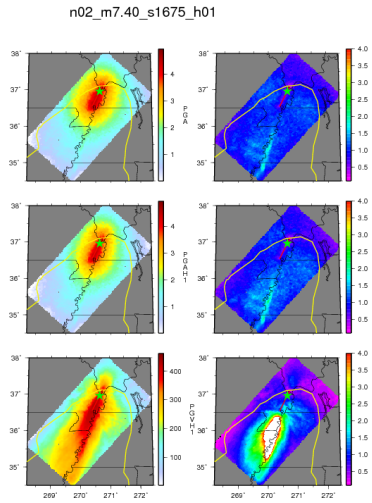

C

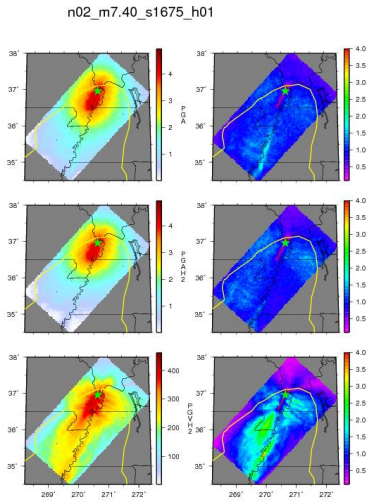

D

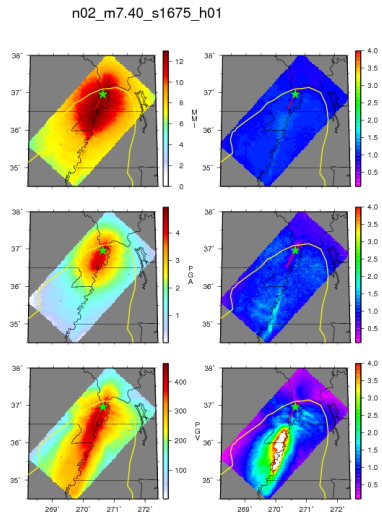

E

Figure 21. Simulated ground motion for rupture model S1675, northeastern fault. Mw is 7.4. For each panel the left column is map of simulated ground motion, and the right column is ground motion after base line trend removed. (A)H1 component of SA at period 3.0sec (top), 1.0 sec (middle) and 0.3 sec (bottom) (B) H2 component of SA at period 3.0sec (top), 1.0 sec (middle) and 0.3 sec (bottom) (C) PGA (top), H1 component of PGA (middle), H1 component of PGV (bottom) (D) PGA (top) H2 component of PGA (middle), H2 component of PGV (bottom). (E) Instrument Intensity (top), PGA (middle) and PGV (bottom).

Basin effects are very obvious, and are superimposed on rupture directivity effects. PGA is strong in a band perpendicular to the fault.

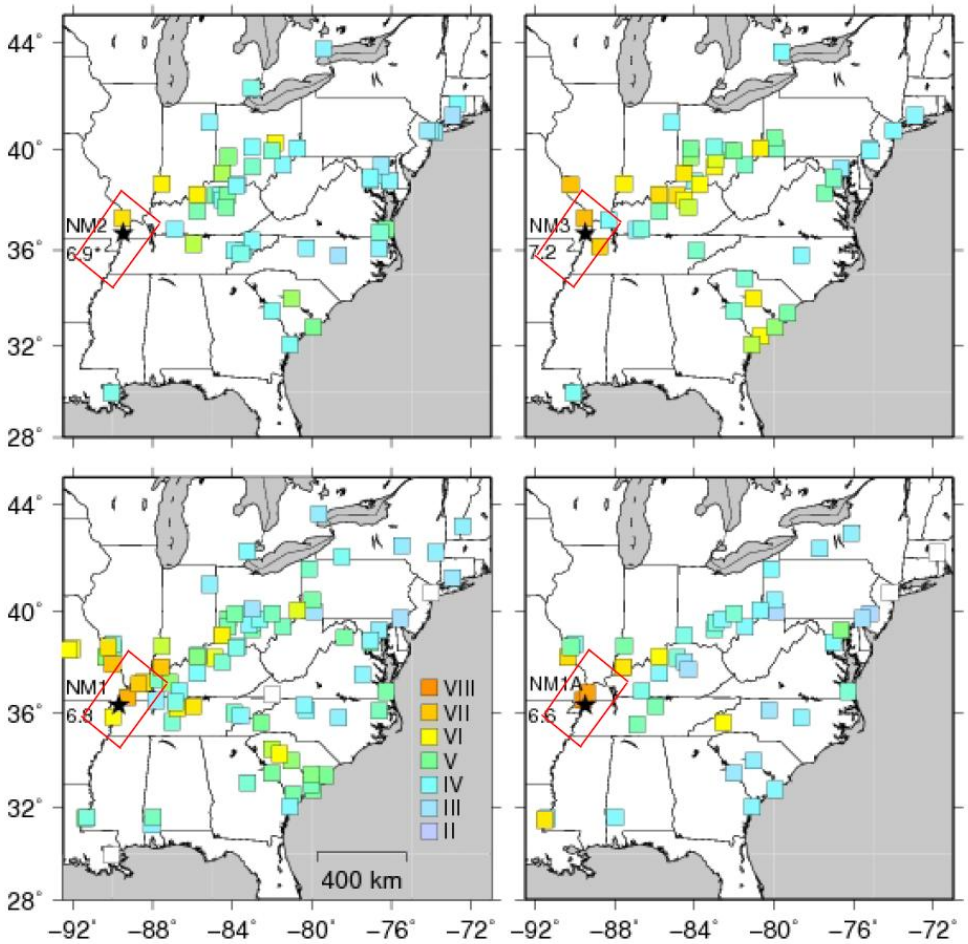

Figure 22. Re-analyzed intensities observation of the New Madrid earthquakes (by Hough and Page, 2011). Red rectangles show target region for ground motion simulation in this project.

6 Discussion

We have simulated ground motion for 9 scenario earthquakes in the New Madrid seismic zone, and the simulation results demonstrate obvious basin effects and rupture directivity effects. However, the target study region is too small (190km x 360km, red rectangle area in Figure 22) to be compared with the intensity observation region (1500kmx1500km) by Hough and Page (2011). Therefore we only compare synthetic and observed intensity in the target region of our project. Hough and Page (2011) mostly observed VII or VI intensity in the area, but our simulations with M7.7 for the southwest fault, M7.6 for the central fault and M7.4 for the northeastern fault show much larger intensity. However, the intensity observations are sparse near the faults, perhaps not dense enough to provide tight constraints on the magnitudes. Moreover, Hough and Page (2011) infer magnitudes from intensity attenuation models for point source earthquakes in CEUS (as used in figure 6 by Hough and Page, 2011). Our simulations show a noticeable discrepancy with the intensity attenuation models. For example, our intensity simulation for M7.7 matches the M7 prediction of the model of Atkinson and Wald (2007). Thus, magnitude estimates based on intensity attenuation models may underestimate the true strength of large earthquakes. To

make a more meaningful comparison between observed and simulated intensity, simulation for a much larger area than ours is needed (Figure 23).

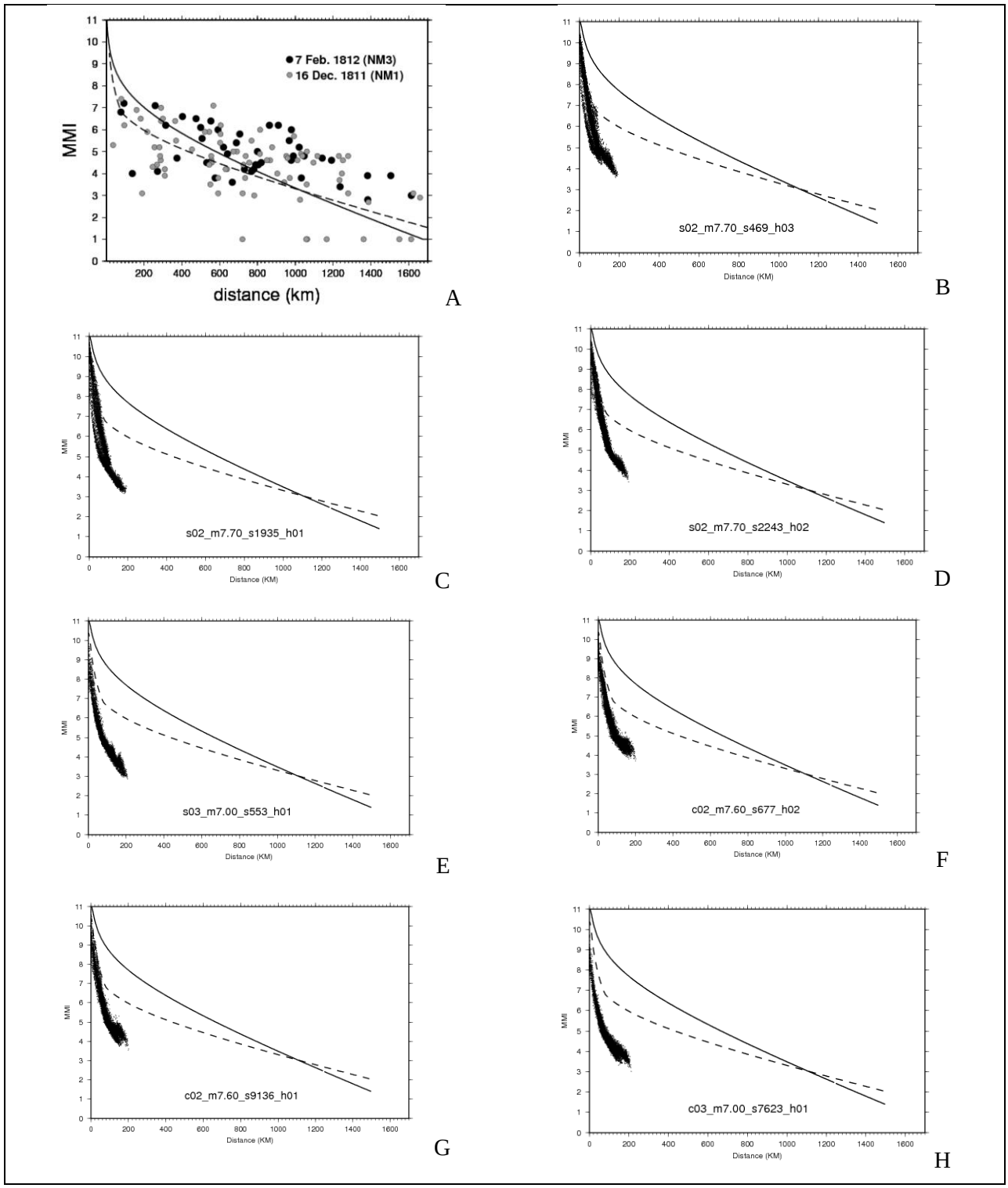

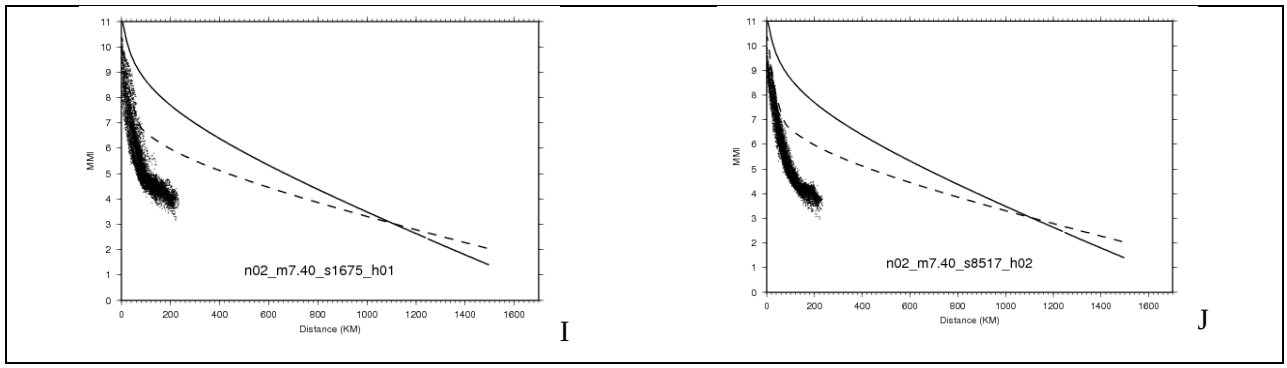

Figure 23. Comparison between observed intensity attenuation vs distance (A) by Hough and Page (2011) and simulated intensity for rupture model (B), Mw7.7 S469,southwest fault (C) Mw7.7, S1935,Southwest Fault (D) Mw7.7, S2243,Southwest Fault (E) Mw7.0,S553,Southwest Fault (F) Mw7.6, S677,central fault (G) Mw7.6,S9136, central fault, (H) M7.0,S7623,central fault, (I) M7.4, S1675, northeastern fault (J) M7.4,S8517, northeastern fault. Prediction lines are for an M7 earthquake based on the models of Bakun et al. (2003) (solid line) and Atkinson and Wald (2007) (dashed line). Our simulation shows a more rapid decrease in intensity, which is probably due to our adoption of a Q value that is not high enough.

DISPOSITION OF DATA SETS

We have generated large numbers of ground motion time histories for New Madrid scenario earthquakes. These time histories are useful to structural engineers who are designing new structures or retrofitting existing structures. For some structures, including base isolated structures and critical structures such as hospitals and emergency management centers, time history analysis may be required for design or retrofit.
The terms of this grant require that all data be made freely available to other investigators. Suites of time histories and response spectra from these scenario events for these types of analyses are available upon request to the PIs.

BIBLIOGRAPHY OF ALL PUBLICATIONS RESULTING FROM THIS PROJECT

Abstracts were presented at the 2010 and 2011 Annual Meetings. A paper is currently being prepared.

ACKNOWLEDGMENTS

Dr. Leo Ramirez-Guzman of the USGS provided valuable help with seismic velocity models. Group discussions with him and as well as Kim Olson and others substantially advanced this project. Dr. Susan Hough kindly provided a preprint of her most recent studies on intensities for the New Madrid earthquakes.

REFERENCES

Aagaard, B. T., T. M. Brocher, D. Dolenc, D. Dreger, R. W. Graves, S. Harmsen, S. Hartzell, S. Larsen, and M. L. Zoback (2008a). Ground-motion modeling of the 1906 San Francisco earthquake, Part I: validation using the 1989 Loma Prieta earthquake, *Bull. Seism. Soc. Am.*, 98, 989-1011.

Aagaard, B. T., T. M. Brocher, D. Dolenc, D. Dreger, R. W. Graves, S. Harmsen, S. Hartzell, S. Larsen, Kathleen McCandless, Stefan Nilsson, N. Anders Petersson, Arthur Rodgers, Björn Sjögreen, and M. L. Zoback (2008b). Ground-motion modeling of the 1906 San Francisco earthquake, Part II: Ground-Motion Estimates for the 1906 Earthquake and Scenario Events, *Bull. Seism. Soc. Am.*, 98, 1012-1046.

Atkinson, G., and I. Beresnev (2002). Ground motions at St. Louis and Memphis from M 7.5 – 8 earthquakes in the New Madrid seismic zone, *Bull. Seism. Soc. Am.* **92**, 1015-1024.

Atkinson, G.M. and D.M. Boore (2006). Earthquake Ground-Motion Prediction Equations for Eastern North America, *Bull. Seism. Soc. Am*. **96**, 2181-2205.

Bakun, W.H., and Hopper, M.G., 2004, Magnitudes and locations of the 1811–1812 New Madrid, Missouri, and the 1886 Charleston, South Carolina, earthquakes: Bulletin of the Seismological Society of America, v. 94, p. 64–75.

Beresnev I. and G. Atkinson (1997). Modeling finite fault radiation from the ω^n spectrum, *Bull. Seism. Soc. Am.* **87**, 67-84.

Boatwright J., and H. Bundock (2005). Modified Mercalli intensity maps for the 1906 San Francisco earthquake plotted in ShakeMap format, *USGS Open File Rpt. 2005-1135*, (**http://pubs.usgs.gov/of/2005/1135**).

Boore D. and W. Joyner (1997). Site amplification for generic rock sites, *Bull. Seism. Soc. Am.*, **87**, 327-341.

Boore, D. (1983). Stochastic simulation of high frequency ground motions based on seismological models of the radiated spectra, *Bull. Seism. Soc. Am.*, **73**: 1865-1894.

Brocher T (2005). Compressional and Shear Wave Velocity Versus Depth in the San Francisco Bay Area, California: Rules for USGS Bay Area Velocity Model 05.0.0, *USGS Open File Rpt. 2005-1317*, (**http://pubs.usgs.gov/of/2005/1317**).

Burger, R.W., P.G. Somerville, J.S. Barker, R.B. Herrmann, and D.V. Helmberger (1987). The effect of crustal structure on strong ground motion attenuation relations in eastern North America, *Bull. Seism. Soc. Am.*, **77**, 420-439.

Campbell, K.W. and Bozorgnia, Y., 2008, NGA ground motion model for the geometric mean horizontal component of PGA, PGV, PGD, and 5%-damped linear elastic response spectra for periods ranging from 0.01 to 10 s, *Earthquake Spectra*, **24**, accepted for publication.

Catchings, R. D. (1999). Regional Vp, Vs, Vp/Vs and Poisson's Ratios across earthquake source zones from Memphis, Tennessee, to Saint Louis, Missouri, *Bull. Seism. Soc. Am.* **89,** 1591–1605.

Cramer, C. (2006). Quantifying the uncertainty in site amplification modeling and its effects on site specific seismic hazard estimation in the upper Mississippi Embayment and adjacent areas, *Bull. Seism. Soc. Am.* **96,** 2008-2020.

Day S. and C. Bradley (2001). Memory efficient simulation of anelastic wave propagation, *Bull. Seism. Soc. Am.*, **91**, 520-531.

Day, S., 1982, Three dimensional simulation of spontaneous rupture: The effect of non-uniform pre-stress, *Bull. Seism. Soc. Am.*, **72**, 1881-1902.

Frankel, A. (1995). Simulating strong motions of large earthquakes using recordings of small earthquakes:the Loma Prieta mainshock as a test case, *Bull. Seism. Soc. Am.*, **85**, 1144-1160.

Graves, R. W. (2004). Validation of simulation methodologies, *Presented at NGA Workshop #5*, Richmond, CA, March 24, 2004.

Graves, R. W. and A. Pitarka (2004). Broadband time history simulation using a hybrid approach, *Proc. 13th World Conf. Earthquake Eng.*, Vancouver, Canada, paper no. 1098.

Graves, R. W. and A. Pitarka (2010) Broadband ground-motion simulation using a hybrid approach, *Bull. Seism. Soc. Am.*, **100**, doi: 10.1785/0120100057.

Graves, R.W. (1996). 3D elastic finite difference modeling of the 1987 Whittier Narrows earthquake. *Proc. 11th World Conf. Earthquake Eng*., Acapulco, Mexico, June 23-28.

Guatteri M, P. M. Mai, G. Beroza and J. Boatwright (2003). Strong ground motion prediction from stochastic-dynamic source models, *Bull. Seism. Soc. Am.*, **93**, 301-313.

Hartzell, S., C. Langer and C. Mendoza (1994). Rupture histories of eastern North American earthquakes. *Bull. Seism. Soc. Am.* 84, 1703-1724.

Hartzell S. and C. Mendoza (2011). Source and Site Response Study of the 2008 Mount Carmel, Illinois, Earthquake, *Bull. Seism. Soc. Am.* ,101, 951-963, doi:10.1785/0120100222

Hartzell, S., S. Harmsen, A. Frankel and S. Larsen (1999). Calculation of broadband time histories of ground motion: comparison of methods and validation using strong ground motion from the 1994 Northridge earthquake, *Bull. Seism. Soc. Am*., **89**, 1484-1504.

Herrmann, R. B., M. Withers and H. Benz (2008). The April 18, 2008 Illinois Earthquake: An ANSS Monitoring Success, *Seism. Res. Lett*., **79**, 830-843, doi: 10.1785/gssrl.79.6.830.

Hough, S., J. Armbruster, L. Seeber, and J. Hough (2000). On the modified Mercalli intensities and magnitudes of 1811–1812 New Madrid earthquakes, *J. Geophys. Res.* **105,** 839–864.

Hough, S. E., and M. Page (2011), Toward a consistent model for strain accrual and release for the New Madrid Seismic Zone, central United States, J. Geophys. Res., 116, B03311, doi:10.1029/2010JB007783.

Hudnut, K., Jones, L., and Aagaard, B., (2007). The southern California ShakeOut scenario, part 1: Earth science specification of a big one, *Seism. Res. Lett*., **78**, 264.

Johnston, A. (1996). Seismic moment assessment of earthquakes in stable continental regions. III. *Geophys. J. Int.* 126, 314–344.

Johnston, A., and E. Schweig (1996). The enigma of the New Madrid earthquakes of 1811–1912, *Annu. Rev. Earth Planet Sci.* 24, 339–384.

Jones, L. M., R. Bernknopf, D. Cox, J. Goltz, K. Hudnut, D. Mileti, S. Perry, D. Ponti, K. Porter, M. Reichle, H. Seligson, K. Shoaf, J. Treiman, and A. Wein (2008). The ShakeOut Scenario, *USGS Open File Report, manuscript in preparation*.

Kelson, K. I., G. D. Simpson, R. B. VanArsdale, C. C. Haraden, and W. R. Lettis, Multiple Holocene earthquakes along the Reelfoot fault, central New Madrid seismic zone, J. Geophys. Res., 101, 6151-6170, 1992.

Kwok, A.O. and Stewart, J.P., 2006, Application of theoretical 1D amplification factors for evaluation of seismic site effects, *Bull. Seism. Soc. Am.*, 96, 1422-1436.

Langston, C. A. (1994). An integrated study of crustal structure and regional wave propagation for southern Missouri, *Bull. Seism. Soc. Am.* 84, 105–118.

Macpherson, K. A., E. W. Woolery, Z. Wang, and P. Liu (2010). Three-dimensional Long-period Ground-motion Simulations in the Upper Mississippi Embayment, *Seism. Res. Lett*., **81**, 391-405, doi: 10.1785/gssrl.81.2.391.

Mai, P. and G. Beroza (2002). A spatial random field model to characterize complexity in earthquake slip, *J. Geophys. Res*., 107(B11), doi:10.1029/2001JB000588.

Nuttli, O. W., The Mississippi Valley earthquakes of 1811 and 1812: Intensities, ground motion, and magnitudes, Bull. Seismol. Soc. Am., 63, 227-248, 1973.

Olsen, K., Day, S., Minster, J., Cui, Y., Chourasia, A., Faerman, M., Moore, R., Maechlin, P., and Jordan, T., (2006). Strong shaking in Los Angeles expected from a southern San Andreas earthquake, *Geophys. Res. Lett*., **33**, L07305.

Petersen, M., A. Frankel, A., S. Harmsen, C. Mueller, K. Haller, R. Wheeler, R. Wesson, Y. Zeng, O. Boyd, D. Perkins, N. Luco, E. Field, C. Wills, and K. Rukstales (2008). Documentation for the 2008 updated of the United States National Seismic Hazard Maps. *U.S. Geological Survey Open File Report* 2008-1128.

Pitarka, A. (1999) 3D elastic finite-difference modelling of seismic motion using staggered-grid with non-uniform spacing. Bull. Seism. Soc. Am., **89**,54-68.

Ramirez-Guzman, L.; Williams, R. A.; Boyd, O. S.; Hartzell, S.,(2010), Central United States Velocity Model Version 1: Description and Validation,American Geophysical Union, Fall Meeting 2009, abstract #S32A-07

Saikia, C.K. and P.G. Somerville (1997). Simulated hard-rock motions in Saint Louis, Missouri, from large New Madrid earthquakes (Mw > 6.5). *Bull. Seism. Soc. Am.* **87**, 123-139.

Saikia, C.K., A. Pitarka and G. Ichinose (2006). Effects of irregular structure of the Mississippi Embayment on ground motion amplification, *Bull. Seism. Soc. Am.* **96**, 1448-1473.

Saikia, C.K., P.G. Somerville, D.V. Helmberger, M.K. Sen, J.P. McLaren, L.J. Burdick, and N.F. Smith (1989). Ground-Motion Attenuation and Earthquake Source Scaling in Eastern North America, Electric Power Research Institute, 307 pp.

Saikia, C.K., P.G. Somerville, H.K. Thio, N.F. Smith, A. Pitarka, B.B. Woods (1998). Crustal structure and ground motion models in the eastern and Central United States from National Seismograph Network Data. NUREG/CR-6593, U.S. Nuclear Regulatory Commission.

Somerville, P.G., J.P. McLaren, C.K. Saikia, and D.V. Helmberger (1990). The November 25, 1988 Saguenay, Quebec earthquake: source parameters and the attenuation of strong ground motion. *Bull. Seism. Soc. Am.*, **80**, 1118-1143.

Somerville, P.G., J.P. McLaren, L.V. LeFevre, R.W. Burger and D.V. Helmberger (1987). Comparison of source scaling relations of eastern and western North American earthquakes, *Bull. Seism. Soc. Am.*, **77**, 332-346.

Somerville, P.G., K. Irikura, R. Graves, S. Sawada, D. Wald, N. Abrahamson, Y. Iwasaki, T. Kagawa, N. Smith and A. Kowada (1999). Characterizing earthquake slip models for the prediction of strong ground motion. *Seismological Research Letters*, **70**, 59-80.

Somerville, P.G., N. Collins, N. Abrahamson, R. Graves and C. Saikia (2001). Earthquake source scaling and ground motion attenuation relations for the central and eastern United States. Final Report to the U.S. Geological Survey, Contract No. 99HQGR0098.

Somerville, P.G., R.W. Graves, N.F. Collins, S.G. Song, S. Ni and P. Cummins (2009). Source and ground motion models of Australian earthquakes. Proceedings of the 2009 Annual Conference of the Australian Earthquake Engineering Society, Newcastle, December 11-13.

Song, S., G. Beroza and P. Segall (2006). A unified source model for the 1906 San Francisco earthquake, *Seism. Res. Lett.*, **77**(2), 271.

Toro, G., and W. Silva (2001). Scenario Earthquakes for Saint Louis, MO and Memphis, TN, and Seismic Hazard Maps for the Central United States Region Including the Effect of Site Conditions, R*isk Engineering, Boulder, Colorado* (*www.riskeng.com*).

Tuttle, M. P., E. S. Schwig, J. D. Sims, R. H. Lafferty, L. W. Wolf, and M. L. Haynes (2002). The earthquake potential of the New Madrid seismic zone, *Bull. Seism. Soc. Am.* **92,** 2080–2089.

Wald, D., B. Worden, V. Quitoriano, and K. Pankow (2005). ShakeMap Manual: Technical Manual, Users Guide, and Software Guide (Version 1.0 Ed.). U.S. Geol. Surv. (available at http://pubs.usgs.gov/tm/2005/12A01/, last accessed February 2008).

Wald, D.J., and T. Allen (2007). Topographic slope as a proxy for seismic site conditions and amplification, *Bull. Seism. Soc. Am.*, **97**, 1397-1395.

Wald, D.J., D. V. Helmberger and T. H. Heaton (1991). Rupture model of the 1989 Loma Prieta earthquake from the inversion of strong motion and broadband teleseismic data, *Bull. Seism. Soc. Am.*, **81**, 1540-1572.

Walling, M., Silva, W.J., and Abrahamson, N.A., 2008, Non-linear site amplification factors for constraining the NGA models, *Earthquake Spectra*, **24**, accepted for publication.

Yaji, Y., 2004, Source rupture process of the 2003 Tokachi-oki earthquake determined by joint inversion of teleseismic body wave and strong ground motion data. *Earth, Planets, and Space* **56**, 311–316.

Zhu, L. and D. Helmberger (1996). Advancement in source estimation techniques using broadband regional seismograms, *Bull. Seism. Soc. Am.*, **86**, 1634-1641.

Zhu L. and L.A. Rivera, 2002, A note on the dynamic and static displacements from a point source in multilayered media, *Geophysical Journal Int.*, 148, 619–627